List of Supplementary Materials

Materials and Methods

Supplementary Text ST1-3

Fig. S1 – S23

Table S1 – S11

Captions for Movies S1 to S10

References (*22-28*)

Materials and Methods

Drosophila genetics

Fly strains used in this study are listed in Table S1. Detailed fly genotypes in each experiment are listed in Table S2-3.

CRISPR knockin of HA tag in mature chemoattractant ligand peptide

Sequences of PVF1, Krn, and Spi were aligned to determine HA insertion sites in the predicted mature peptide after cleavage (Tables S4). gRNA was designed (http://targetfinder.flycrispr.neuro.brown.edu/) after sequencing the host genomic DNA and cloned into the pU6-BbsI-chiRNA vector (Tables S5-6). HA tag insertion was designed according to scarless editing (https://flycrispr.org/scarless-gene-editing/) by cloning ~1kb left and right recombination arm into the pHD-2xHA-ScarlessDsRed vector. Primers used were listed in Table S7. CRISPR injection was performed by BestGene into fly strains expressing Cas-9 in the germ-line (Table S1 and S8). Individual F1 was crossed with PBac to remove scarless, and screened by eye color. Genomic DNA was extracted and sequenced to verify correct insertion. Egg chambers were stained live or fixed to detect HA signals (Table S8).

Egg chamber dissection and staining

Adult female ovaries were dissected in Schneider’s Drosophila medium (Thermo Fisher Scientific, Waltham, MA; 21720) with 20% fetal bovine serum. Ovarioles containing egg chambers of the desired stages were pulled out of the muscle sheath with #55 forceps.

For fixed sample staining, ovarioles were then fixed for 20 min in 4% paraformaldehyde at 4 °C. For lectin (Lectin PNA Alexa 647; Thermo Fisher Scientific; L32460) staining, ovarioles were incubate in dissection medium containing 10 μg/ml lectin for 3 min before fixation. After fixation, ovarioles were washed with PBS/0.4% Triton X-100 (PBST), and then incubated with primary antibodies overnight at 4 °C. The following day, ovarioles were washed with PBST before incubation in secondary antibody for 1.5 h. After removal of secondary antibodies, samples were stained with Hoechst for 20 min. Samples were stored in VECTASHIELD (Vector Laboratories, Burlingame, CA) at 4 °C.

For HA-Keren live staining, egg chambers older than stage 10 were removed, and ovarioles incubated in live imaging medium containing insulin and anti-HA DyLight 550 (Thermo Fisher Scientific; 26183-D550) and Alexa-Fluor 647 (to mark non-specific trapping of antibodies in extracellular spaces) for 30 min. They were quickly rinsed two times with dissection medium and immediately mounted for live imaging. For dextran live labeling of extracellular space, dextran is membrane impermeant and readily diffuses between cells, but is endocytosed over time. Therefore we incubated living egg chambers in fluorescently labeled dextran (100 μg/ml; Dextran Alexa 647 10,000 MW; Thermo Fisher Scientific; D22914) and imaged them immediately, before endocytosis could occur.

Additional antibodies/dyes used in this study: rat anti-Ecad from Developmental Studies Hybridoma Bank (DSHB, Iowa City, IA; DCAD2; 1:50), chicken anti-GFP (Abcam, Cambridge, UK; 13970; 1:2000), Phalloidin for F-actin (Sigma-Aldrich; 65906; 1:1000).

Confocal imaging and visualization

For confocal z-stack imaging, in order to preserve the 3D structure and keep the sample stable during imaging, we adjusted the mounting and z-stack imaging method. First, for mounting, we used an 18 mm x 18 mm coverglass on the top and a 22 mm x 40 mm coverglass on the bottom for the inverted microscope to minimize sample movement by the touching objective during z-stacks. Four ~0.5 mm X 0.5 mm No.1 coverglass debris were used as bridges on four corners to avoid crushing of the egg chambers. 48.6 ul VECTASHIELD were used to allow 150 μl gap between the two coverglases so that the egg chambers were not compressed. Second, for imaging, we used a 40× 1.1 N.A. 0.62mm long working distance water objective on a Zeiss LSM780 confocal microscope. Laser power corrections were applied by increasing the laser power as the objective scans from the near end of the sample to the far end of the sample.

Confocal z-stack images were visualized in Imaris (Bitplane, South Windsor, CT), Representative images were exported from Imaris using either 3D view or slice view. In Fig. 2E and F, fig. S10A, and fig. S14A, nurse cell nuclei signals were masked to aid visualization of the membrane signals. In Fig. 3F, fig. S13E and F, and fig. S17B, dextran signals outside of the egg chamber were masked to aid visualization of signals inside. Exported images were rotated and cropped in Photoshop (Adobe, San Jose, CA). Single channel images were converted from a black background to a white background using Invert LUT function in FIJI. Rainbow display of migration was generated using a subset of live image MIPs colored in FIJI using a custom LUT.

Quantification in 2D, 3D and 4D

Keren Quantification: Antibodies can accumulate non-specifically in extracellular spaces and be endocytosed by follicle cells including border cells. In order to correct for non-specific fluorescent signals, we incubated egg chambers in both HA-Keren and Alexa-Fluor 647 antibodies. The non-specific \ Alexa-Fluor 647 fluorescence was subtracted from the HA-Keren total fluorescence to yield the specific anti-HA signal. Final analysis was performed on the subtracted image of HA-Keren minus Alexa-Fluor 647. The intensity of the Alexa-Fluor 647 channel was attenuated by a factor calculated by comparing relative signal strength between HA-Keren and Alexa-Fluor 647, so that the subtracted HA-Keren retained a basal intensity. In order to quantify the anterior-posterior signal, we used FIJI to draw a line perpendicular to the membrane 30 pixels wide to capture the full width of the local nurse cell contact. We moved this line along the anterior-posterior axis to capture different positions. In order to quantify the medial-lateral signal we started from the lateral edge of a nurse cell membrane path and moved the line towards the center using the same method described above. We excluded curved or fuzzy membranes and focal planes that included ring canals. Raw distance was converted to the relative 0%-100% position along each axis. Each data point of medial-lateral signal was normalized to the average within each egg chamber. The ML gradient slope was calculated from n=6 of each genotype and from 0-100% medial position. Each data point of anterior-posterior signal was normalized to the average of data points located between 40%-60% of the anterior-posterior migration path because every egg chamber included data points from this region. Data points from six to seven egg chambers are shown for each genotype. A fitted line represents the trendline of normalized Keren distribution along the anterior-posterior or medial-lateral axis. The standard deviation of the best fit trendline was represented by color shades in the graph. The AP slope was calculated from normalized intensity between 0%-70% the distance from the anterior tip to the oocyte from three shgRNAi egg chambers and four control egg chambers all of which included data points from 0%-70%. The P values were based on t test comparisons of the AP and ML slopes.

For quantification of posterior and medial migration indices in 3D, we used Imaris MeasurementPro in the following steps: 1) use an Oblique Slicer across the center of the nurse cell-ooctye border to set a plane parallel to the posterior follicle cell ring, set point B at the center of the nurse cell-oocyte border (fig. S1A); set point A at the anterior end of the egg chamber (Line AB measures and length of the anterior-posterior distance in nurse cells where border cells need to migrate); 2) move the previous Oblique Slicer going across the center of the border cell cluster, set point C at the intersection of the plane and line AB (Line AC measures how much border cell migrates from anterior); 3) on the Oblique Slicer plane that goes across C, set point D at the center of the border cell cluster, set point E and F at the edge of the egg chamber such that line EF goes through both the center of the cross sectional plane and the center of the border cell cluster (Line EF measures diameter of the egg chamber where the border cell is at). Posterior migration index = AC/AB * 100%; Medial migration index = min (DE, DF)/(EF/2) * 100%.

Posterior migration was quantified in stage 10 egg chambers. Note that in nurse cell Ecad knockdown, centripetal cells show migration defects so they are not used for staging. Instead, egg chamber size and nurse cell:oocyte volume ratio were used to identify stages 9 and 10. Medial migration was quantified in stage 9 egg chambers in which border cells had migrated 25-75% of the way to the oocyte border, where the abundance of alternative paths is greatest, except where otherwise specified (e.g. fig. S22 where we analyzed 75-100%). The preference for multiple nurse cell junctures was also evident at the initiation of migration (fig. S23).

For quantification of nurse cell membrane deflections in 3D, we used Imaris FilamentTracer in the following steps: 1) egg chamber drift in time was corrected by locating a few immobile anterior stretched cells, stalk cells, and posterior columnar cells using the Spots function in Imaris Track based on Ubi-HisRFP; 2) The same 3-cell juncture was tracked in each time frame using the AutoDepth method in Filaments based on the UMAT-Lyn-tdTomato signal, and were trimmed to ~8 µm length; 3) The Dendrite Orientation Angle was exported and used to calculate the membrane deflection angle.

For quantification of ≥3-cell juncture density in 3D, we used Imaris MeasurementPro in the following steps: 1) rotate the egg chamber so that it is not tilted in Z and the anterior is towards the left; 2) measure the anterior tip and the oocyte border position X, and then calculate 20, 30, 40, 50, 60, 70, 80% locations in X; 3) set a YZ Ortho Slicer in the each of these planes, add Measurement Points at the center of each YZ plane, as well as all the 3-cell junctures (Fig. 3B, blue dots); 4) in 3D view, trace all 3-cell juncture lines using Filament, and place Spots at the junctures of those filaments as >3 cell junctures (Fig. 3A, magenta dots); 5) export statistics for position XYZ, then calculate the distance to the center in the YZ plane; 6) bin the data in 5 µm radius intervals, and plot the heat map.

For quantification of dextran-labeled free space in 3-cell junctures (fig. S13G), we measured their diameter in 2D. An oblique slicer was used to find the 3-cell junctures that were close to the objective and almost parallel to the imaging plane to minimize the distortion from out-of-focus light. The line width of the 3-cell junctional space was measured from the slice using FIJI. Dextran-labeled free space in >3-cell junctures were measured in 3D. We used Imaris MeasurementPro Surface function and exported Volume statistics.

For quantification of 2-cell surface contact area in 3D, we used Imaris Cell function in the following steps: 1) rotate the egg chamber in 3D so that it is not tilted in Z and perform attenuation correction to adjust membrane signal intensity in Z; 2) Locate border cells, nurse cells, and oocyte nuclei using Spots function, add an additional Spot outside of the egg chamber, mask the nuclei stain channel with the Spots; 3) segment border cells, nurse cells, and oocyte using the Cell function by two channels, the masked nuclei channel and the membrane channel; 4) export Cells to Surfaces, and split nurse cell membrane surfaces and label them according to the identify in fig. S11A, S16A and S21C; 5) run Surface surface contact Macro in ImarisXT to segment different surface contact; 6) group them according to their location, and export statistics for the Area.

For quantification of the protrusion frequency in 4D, we did in the following steps: 1) manually set Spots at the tip of the protrusion by rotating the border cells in 3D in each time frame; 2) use an Oblique Slicer going perpendicular to the protrusion to determine if the protrusion is located at 2-cell interface or 3-cell juncture; 3) record the type of protrusion across the time frames.

For quantification of border cell cluster migration speed in 4D, we followed a published protocol (*22*): 1) egg chamber drift in time was corrected as described above; 2) border cell cluster was tracked using the Surfaces function in Imaris Track based on slbo-4XPHEGFP; 3) instantaneous speed was exported and plotted.

Light sheet imaging and data processing

For light sheet imaging, younger and older egg chambers in the same ovariole of the targeted early stage 9 egg chamber were removed carefully with sharp forceps so they do not block the light path. The desired egg chambers were mounted in 0.5% low melting point agarose with fluorescent beads (Thermo Fisher Scientific; T7280) in 0.68 mm diameter capillary (Zeiss; 701902). Egg chambers that are oriented vertically in the capillary were chosen for imaging to minimize light blocking effect from the opaque oocyte. Images were taken from 8 angles 45 degrees apart on a Zeiss Lightsheet Z.1.

Images were registered, fused and deconvoluted using the Multiview-Reconstruction FIJI plugin (*23*). The fused and deconvolved egg chambers were then segmented into different germ cells using the Imaris Cell software and exported as surfaces. We then imported the surfaces into Meshlab to clean up the mesh as well as generate a PLY file that can be analyzed using Tissue Cartography (*24*). This was done by the following Meshlab commands: 1) importing the cell surface; 2) poisson disc sampling with base mesh subsampling; 3) computing normals for point sets; 4) surface reconstruction: poisson. The reconstructed surface is then exported as a PLY file. The PLY file was then analyzed using Tissue Cartography, details provided in the reference above. In short, the mesh is used to define the center of a region of interest. We then look at a sum of all of the pixels within a 1.5 um distance from the mesh. This signal is then “pulled-back” into a 2D image that can be analyzed using standard processing techniques. These 2D images were manually segmented and quantified in FIJI. Surfaces containing ring canals were not analyzed, due to both higher signal in the ring canal structure, and lower signal within the ring.

FRAP imaging and data processing

Fluorescence recovery after photobleaching (FRAP) was done using a homozygous viable GFP trap line in the shotgun (Ecad) locus. Egg chambers were dissected in Schneiders media supplemented with 0.4 mg/mL insulin (Sigma) and 1X antimycotic/antibiotic (Gibco) before mounting on lumox dishes. FRAP performed using an inverted Zeiss LSM800 confocal microscope fitted with a Plan-Apochromat 40X, 1.2

NA multi-immersion objective with the collar set for water immersion. The Zeiss Zen software bleaching module was used to bleach a 3x5 μm rectangle of nurse cell membrane for 10 iterations using a 10 mW 488 nm diode laser with 3.1 mW at the sample plane. Image capture settings were as follows: 512x512 pixels (79.86 μm^2 in XY) with a 316 msec scan time (1.03 μsec pixel dwell) using a 3.93 Airy unit or 3.2 μm section thickness at a bit depth of 16. A total of 5 pre-bleach images were taken at a 2.5 sec interval followed by 3 min of post-bleach imaging at the same 2.5 sec imaging interval. Fluorescence intensity was measured for the bleached membrane region, a non-bleached control membrane region and a background region outside of the egg chamber. These values were then input into the easyFRAP web application (https://easyfrap.vmnet.upatras.gr) to calculate the $T_{1/2}$ and mobile fraction of E-cadherin on side versus center nurse cell membranes. Graphs were then processed in Prism (GraphPad, La Jolla, CA).

Statistics and reproducibility

All fly crosses were repeated at least twice and ovary dissections and staining were repeated at least three times. Data describe technical or biological replicates. Sample size was not predetermined by statistical methods but we used prior knowledge to estimate minimum sample size. Samples of the correct stage were included and no data point that fits the analysis criteria was excluded. The experiments were not randomized. Investigators were not blinded.

Standard statistical tests were performed using Prism. Sample sizes were appropriately large with appropriate distributions. Mann–Whitney nonparametric test (two-tailed) was used for comparing two groups with different variance. Kruskal–Wallis nonparametric test, followed by Dunn's multiple comparisons test was used when the variance is significantly different among multiple groups. Paired t-test (two-tailed) was used for comparing the two measurements from the same sample.

Data and code availability

The authors declare that all data and code supporting the findings of this study are available within the article and its supplementary information files or from the corresponding author upon reasonable request.

Supplementary Text

ST1. The free space in 2D and 3D

To determine the possible free space in a N-cell juncture, we assume that the equilibrium configuration is determined by a balance between the adhesion energy between nurse cells (parameterized by A, per unit length in 2D, and per unit area in 3D) and the membrane/cortex bending energy (parameterized by bending modulus B, per unit length in 2D and per unit area in 3D). First, we consider the 2D case shown in fig. S13 A and B for $N = 3$and $N = 4$. The geometry of the junctures is characterized by circular arcs of membrane with radius R_f that join smoothly, i.e. without creating a cusp. The system's energy reaches a minimum when $\delta(W_{adh} + W_{bend})/\delta R = 0$. The bending energy for each arc is computed by integrating over the angle of polygon $(N - 2)\pi/N$ (for the examples shown in fig. S13A and B this angle is $\pi/3$ and $\pi/2$, respectively). Computing the energy change for each arc, we arrive at $\delta W_{bend} =- BN\theta(N)\delta R/R^2$ with $\theta(N) = (N - 2)\pi/N$. Due to the change in R the total length of cell-cell contact changes and the resulting total change in adhesion energy is $\delta W_{adh} = NA\delta L = N(A\cot[\theta(N)/2]\delta R)$. Setting $\delta(W_{adh} + W_{bend}) = 0$ we find for the equilibrium radius

$$R_f^2 = B(N - 2)\pi\tan(\pi/N)/(NA).$$

The area of the free space is then the area of the N-polygon connecting the circle center minus the area of the circular sectors. The area of the polygon is $NR_f^2\cot(\pi/N)$while the area of sectors is $N\theta(N)R_f^2/2$. Thus, the total free space is given by

$$S_{free} = S_{polygon} - N\theta(N)R_f^2/2 = [N\cot(\pi/N) - (N - 2)\pi/2]B(N - 2)\pi\tan(\pi/N)/(NA)\equiv f(N)B/A$$

.

In fig. S13C we show that $f(N) = S_{free}/(B/A)$is a monotonically increasing function of N. This indicates that the available space becomes larger as the number of cells in the juncture increases. Note that $S_{free} \sim B/A$ which predicts that, as adhesion decreases, the free space in cell junctures increases, which is consistent with the results of the E-cadherin knock-down experiments (fig. S13E to G).

Following the same argument, the above calculation can be directly extended to 3D, where the nurse cell membranes, now considered to be spherical caps, join smoothly at the juncture. Unlike 2D, where any number of arcs can join to form a polygon, in 3D the stacking of spherical caps is more complicated. Specifically, it is only possible for N=4,6,8,12, and 20, such that the center of the spheres form a polyhedron known as a Platonic solid. The N=4 example, resulting in a tetrahedron, is shown in fig. S13D. We again have the adhesion-bending $\delta(W_{adh} + W_{bend})/\delta R = 0$, where close at $\delta W_{adh} = ANR\delta R\cot[\theta(N)/2]$ and $\delta W_{bend} =- BN\phi(N)\delta R/R^3$. Here, $\theta(N)$ and $\phi(N)$is the dihedral angle and the solid angle of the face of the polyhedron, respectively. The equilibrium radius is thus

$$R_f^4 = B\phi(N)/(A\cot[\theta(N)/2])$$

The free space volume is the volume of the Platonic solid minus the volume of the spherical caps,

$$V_{free}(N) = V_{solid}(N) - NR_f^3(N)\phi(N)/3.$$

For N=5, a simple configuration is mirror imaging a tetrahedron (N=4), which gives $V_{free}(5) = 2V_{free}(4)$. For N=7, there is no simple stacking. The ratio of the free space volume between N=4,5,6, and 8 in 3D is 1 : 2 : 6.6 : 11.6, which increases as N increases. This is close to the experimental ratio, which was found to be 1 : 3.8 : 9.5 : 15.5 (Fig. 3G, the middle point is arbitrary and is scaled to match the experimental data). As a comparison, the ratio in 2D is N=4,5,6,8 is 1 : 2.3 : 3.8 : 7.4.

ST2. Energy costs of protrusions

When border cell protrusions extend into a two-nurse-cell juncture, they have to "unzip" the adhesion bonds between nurse cells. Additionally, there is an energy cost due to the need to bend nurse cell membranes (Fig. 3E, orange box). The adhesion penalty is approximately $W_{adh,2} = 2\pi r A \approx AP$, where $r$is the average radius of the border cell protrusion and P is its perimeter. The bending penalty is $W_{bend,2}{\approx}2\pi B/r$. When border cells protrude into $N{\geq}3$ cell junctures, the protrusions break fewer adhesion bonds due to the pre-existing space, so the adhesion penalty is smaller than in two cell junctures. Furthermore, in contrast to the two-cell juncture, squeezing into $N{\geq}3$should *release* bending energy, by reducing the nurse cell curvature from $1/R_f$ to $1/R_p$, where R_f and R_p represent the local radius of the nurse cell membrane before and after the protrusion moves in (Fig. 3E, cyan and magenta boxes). In general, $R_p > R_f$. The adhesion penalty is proportional to the nurse cell membrane that must be unzipped, given by $W_{adh,N} = A(N - 2)\pi(R_p - R_f)$. The difference of total bending energy is $W_{bend,N} = B(N - 2)\pi(1/R_p - 1/R_f)$. In the simple case, we can model border cell protrusions in full contact with the nurse cells with a fixed perimeter of $(N - 2)\pi R_p = P$. Note that, in this case, the adhesion difference due to nurse-border cell contacts is independent of N. Then,$W_{adh,2} > W_{adh,N}$ and $W_{bend,2} > 0 > W_{bend,N}$for $N{\geq}3$. Thus, both bending and adhesion energies favor protrusion into $N{\geq}3$ -nurse-cell junctures rather than into two-cell junctures. Furthermore, $W_{adh,N} = A(N - 2)\pi(R_p - R_f) = AP - A(N - 2)R_f$ decreases as N increases. Values of $W_{adh,N}$are listed in Table S9.

Furthermore, we estimate the value of $B/A{\approx}1\ \mu m^2$by fitting the experimental data in Fig. 3G with the free space volume ratio in 3D. The relative contribution from adhesion and bending energy can be found from $|W_{bend,N}/W_{adh,N}| = \frac{B}{A|R_p R_f|} \approx \frac{\sqrt{B/A}}{R_p\sqrt{(N-2)\pi\tan(\pi/N)}}$. $R_p$can be estimated from the size of the border cell protrusions $r = R_p\tan(\frac{\pi}{N})$. From experimental data, we can estimate $r \approx 2\mu m$(fig. S14B). Plugging the estimates we get $|W_{bend,N}/W_{adh,N}| \ll 1$for $N{\geq}3$, which indicates that the bending energy is negligible compared to the adhesion energy.

ST3. The 3D dynamic model

To understand the dynamics of border cell cluster migration in response to physical and chemical cues, we developed a dynamic model that describes the trajectory of border cells within an experimentally determined three-dimensional topography of egg chambers. A complete physical model would describe border cells as deformable 3D objects that exert forces on each other and on deformable nurse cells, and that migrate through a complex 3D geometry guided by chemotactic and geometric cues. Such a model is currently not feasible. We, therefore, model the border cell cluster as a point particle, representing the center of mass, that moves in a 3D geometry based on experimental data, and that follows experimentally derived rules. This model allows us to probe the relative importance of topographic and chemotactic cues.

The mass center of the border cell cluster is modeled as a particle located at position $\vec{r}$ moving in an effective potential $U(\vec{r})$ and subject to noise $\zeta(\vec{r}, t)$. The motion can be described by an overdamped stochastic Langevin equation

$$d\vec{r}/dt =- \nabla U(\vec{r}) + \zeta(\vec{r}, t),$$

where $< \zeta(\vec{r}, t)\zeta(\vec{r}', t') >= 2\ \delta(\vec{r} - \vec{r}')\delta(t - t')$. The effective potential incorporates the different guidance terms:

$$U(\vec{r}) = \alpha D(\vec{r}) + \beta_1 S_1(\vec{r}) + \beta_2 S_2(\vec{r}).$$

The topographic cue is described by the first term. It takes into account that the border cells have multiple protrusions which probe their surroundings. The border cell cluster is more likely to move into places where more free space is available. We model this by including the average energy cost in a sphere of cluster size

$$D(\vec{r}) = \int W(\vec{r})\Theta(r_0 - r\ )d\vec{r} / \int \Theta(r_0 - r\ )d\vec{r}.$$

Here $\Theta(r_0 - r\ ) = 1$when $r_0 > r$, otherwise $\Theta(r_0 - r\ ) = 0$, $r_0$is the average radius of the border cell cluster, and $W(\vec{r}) = W_{adh}[N(\vec{r})] + W_{bend}[N(\vec{r})]$, where W_{adh} and W_{bend} are the energy costs of protruding into a N-cell juncture at position $\vec{r}$ (computed in ST2). Note that $D(\vec{r})$ has a dominant weight to the outer surface of the cluster where protrusions are formed.

The chemotactic cues are described by the second and third term and take into account chemoattractant gradients along the anterior-posterior and dorsal-ventral axis. Along the anterior-posterior axis, we use, following (*25*), an exponential concentration profile: $S_1(\vec{r}) = c_0 + (c_m - c_0)\exp[-\ (x - L)/\xi]$, where ξ is the length scale of the exponential profile decay, and L is the total length of the egg chamber. Dorsal-ventral guidance is incorporated by a concentration gradient of the protein Gurken, which we represent as $S_2(\vec{r}) = c_2[d_0 - d(x, y, z)]$, where $d(x, y, z) = \sqrt{(x - x_0)^2 + (y - y_0)^2 + (z - z_0)^2}$ is the distance to the Gurken source. Earlier studies revealed that this guidance is only relevant near the posterior of the egg chamber and thus only exists in our model when $x > 2L/3$ (*5*). Furthermore, we assume that nurse cells represent static obstacles such that $U(\vec{r}) = \infty$ when $\vec{r}$ falls within a nurse cell. Finally, the strength of the geometric cue and chemotactic cue is determined by the parameters α, β_1 and β_2.

In our simulations, we first discretized space in an experimentally segmented egg chamber, resulting in a cubic grid of 1µm. Each grid point is assigned with an identity which indicates the juncture type it belongs to (e.g., 2 or 3-cell juncture). Our simulations started by placing the particle (i.e., border cell cluster) at the anterior end of the egg chamber. We then incorporated a discrete version of the Langevin equation in which, for each time step, the particle can move to a neighboring cubic grid points with probability

$$p(\vec{r} \rightarrow \vec{r} + \Delta r) = Z^{-1}\exp\{[U(\vec{r}) - U(\vec{r} + \Delta r)]\},$$

where $Z = \sum_{\Delta r} \exp\{[U(\vec{r}) - U(\vec{r} + \Delta r)]\}$ is the partition function, and the sum is over all nearest neighbors of position $\vec{r}$. The potential can be parameterized by rescaling units such that $A = 1$ (notice that the bending energy is negligible, as shown in ST2). The simulation was terminated when the particle reached the oocyte or the total number of simulation steps exceeded 10^4(a typical simulation in wild type egg chamber takes $\sim 10^3$ steps.). Parameters used in the model are given in Table S10. For different combinations of α and β, the mediolateral and anteroposterior indices are shown in Table S11.

Our model can also be applied to the case when E-cadherin is knocked down. In the E-cadherin knockdown egg chamber, the nurse-follicle cell junctures are 2.5 fold larger than the wild type nurse-follicle cell juncture (fig. S13F and G). This difference in juncture size indicates that the adhesion between nurse cell and follicle cells is smaller (see section above). In our simulation, we set $A = 0.4$ while keeping the other parameters the same.

Supplementary Figures and Legends

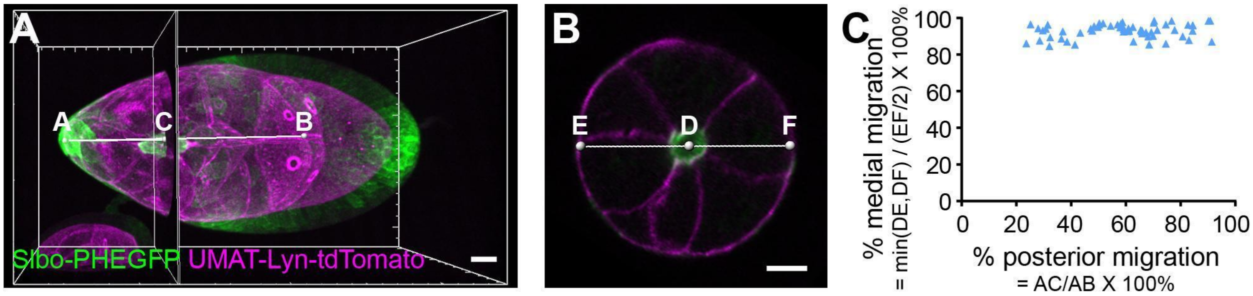

Fig. S1. 3D analysis reveals orthogonal anteroposterior and mediolateral pathway choices

(A) Lateral view showing the method for quantification of posterior migration. (B) Cross sectional view showing the method for quantification of medial migration. (C) Migration in control stage 9 egg chambers. The cells remain in the center as they move from anterior to posterior (n = 59 egg chambers). Scale bars, 20 µm.

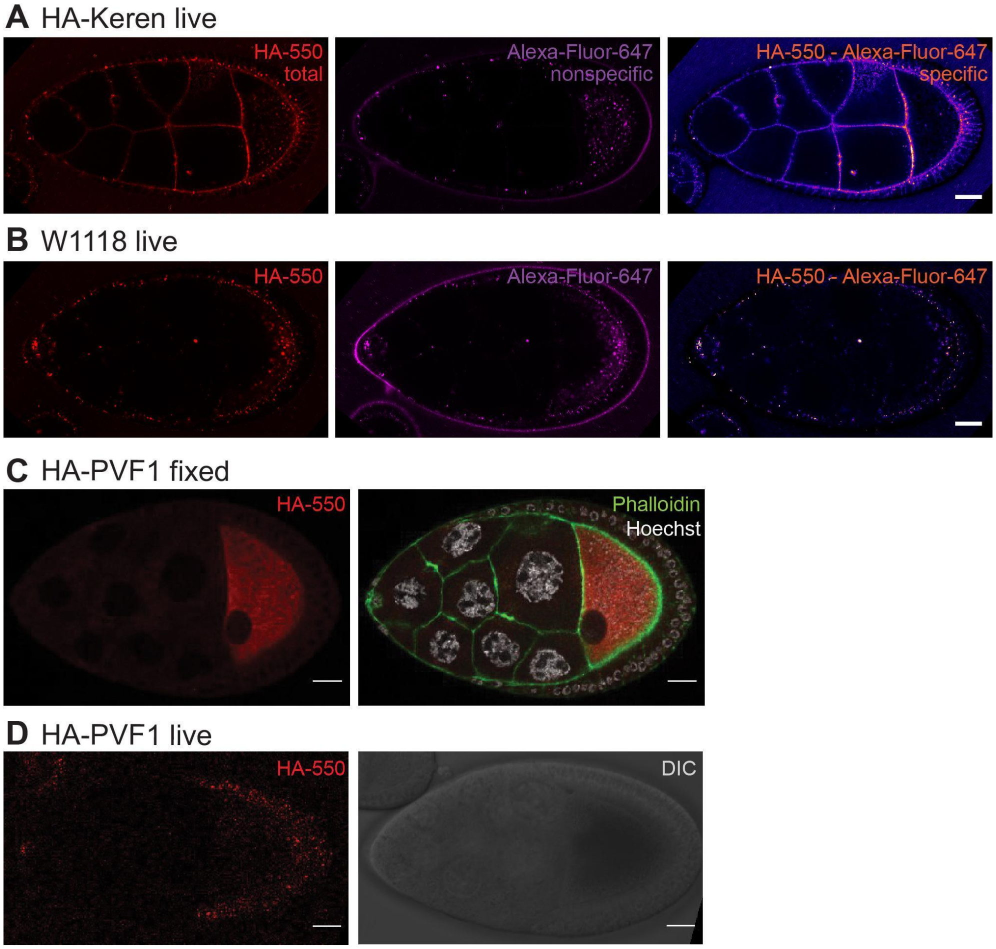

Fig. S2. HA tagging chemoattractant staining

(A) Staining of a living stage 9 egg chamber from a homozygous CRISPR HA-Keren fly with anti-HA-550 (left panel) and a non-specific Alexa-647 antibody (middle panel). The specific HA-Krn signal (right panel) was calculated by subtracting the non-specific Alexa-647 fluorescence from the total anti-HA-550 fluorescence (see methods for details). (B) Staining of a stage 9 egg chamber from w1118 (negative control) with the same antibodies as in A. (C) Staining of a fixed and permeabilized stage 9 egg chamber from a homozygous CRISPR HA-PVF1 fly with anti-HA-550 antibody alone and with Hoechst for DNA (white) and Phalloidin for F-actin (green). (D) Staining of a living stage 9 egg chamber from a homozygous CRISPR HA-PVF1 fly with anti-HA-550 showing that extracellular PVF1 is not detected, though the tagged protein is functional because homozygous flies are viable and fertile (Table. S8). DIC imaging of the same egg chamber is shown. Scale bars, 20 μm.

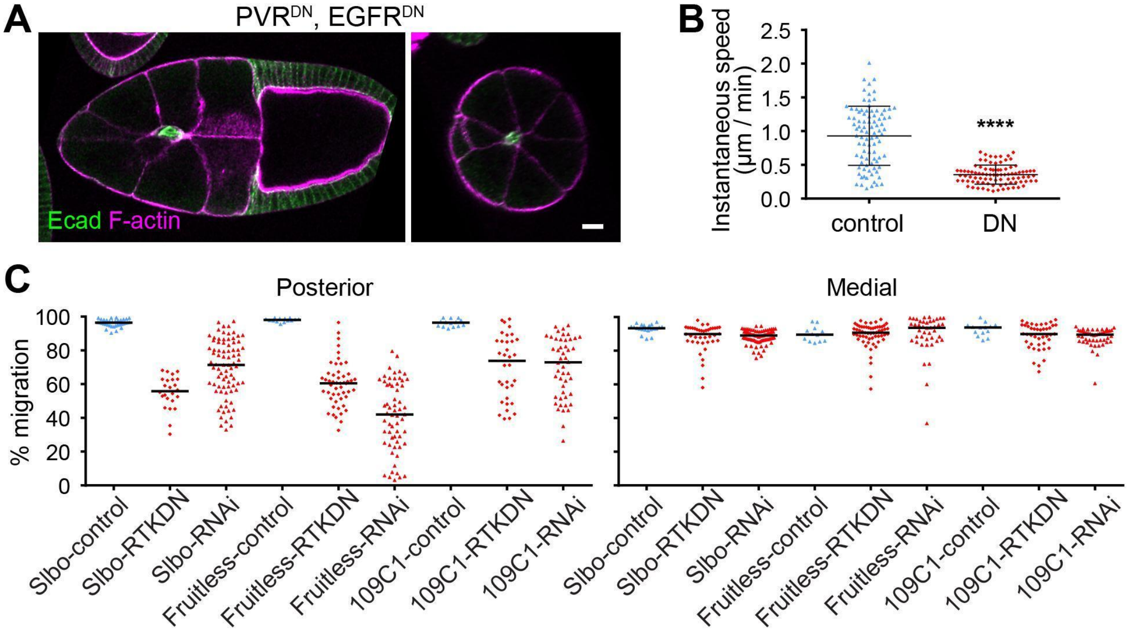

Fig. S3. Migration defects caused by PVR and EGFR RNAi or dominant-negatives (DN)

(A) Lateral and cross sectional views showing an example of posterior migration defect but normal mediolateral path selection in slbo-Gal4>UAS-PVR^{DN}, EGFR^{DN}. Scale bars, 20 µm. (B) Quantification of instantaneous migration speed during early stage 9, in 2 minute time intervals over the course of one hour in slbo-Gal4 control or slbo-Gal4>UAS-PVR^{DN}, EGFR^{DN} . Data from $n = 90$ time points (30 time points each from 3 egg chambers per group). ****, $P < 0.0001$ (Mann-Whitney test). Reduced migration speed shows the dominant-negative receptors were effective. (C) Quantification of migration index following expression of EGFR^{DN} and PVR^{DN} (RTK^{DN}) with the following Gal4 lines: Fruitless-Gal4 expresses in border cells from stage 4, 109C1-Gal4 from stage 7, slbo-Gal4 from stage 8.

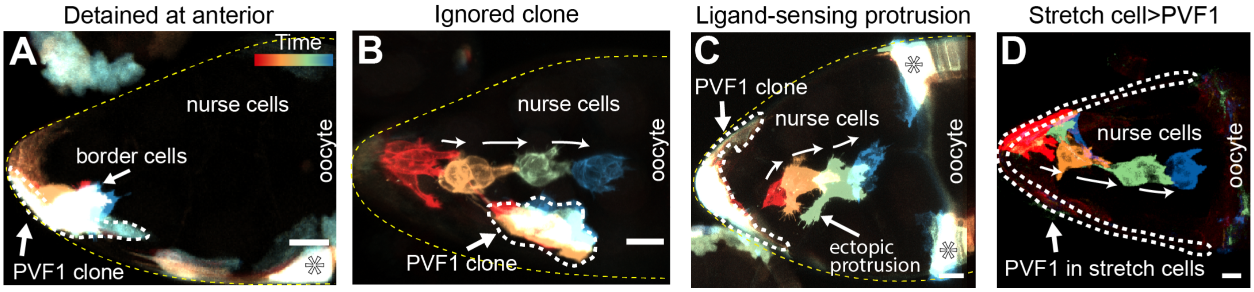

Fig. S4. Border cell cluster responses to ectopic clones of PVF1 expression

(A) Border cells detained at the egg chamber anterior by a clone of PVF1-expressing cells (n=6), confirming that they sense PVF1 from the clone. (B) Border cells protrude toward an ectopic PVF1 clone yet take the central path (n=6). (C) Border cells extend ectopic protrusion towards PVF1 clones. PVF1 clones are marked by hsFlp, AyGal4>UAS-GFP, and border cells are marked by Slbo-PHEGFP. Selected time points from live imaging are pseudo-colored by time from red (early) to blue (late). Stationary cells appear white. (D) PVF1 over-expression in anterior, “stretch” follicle cells. White dashed lines outline PVF1-expressing cells. Yellow dashed lines in A-C outline the anterior part of the egg chamber. Oocyte and nurse cell positions are indicated. Asterisks in A and C denote centripetal cells. Scale bars, 20 μm.

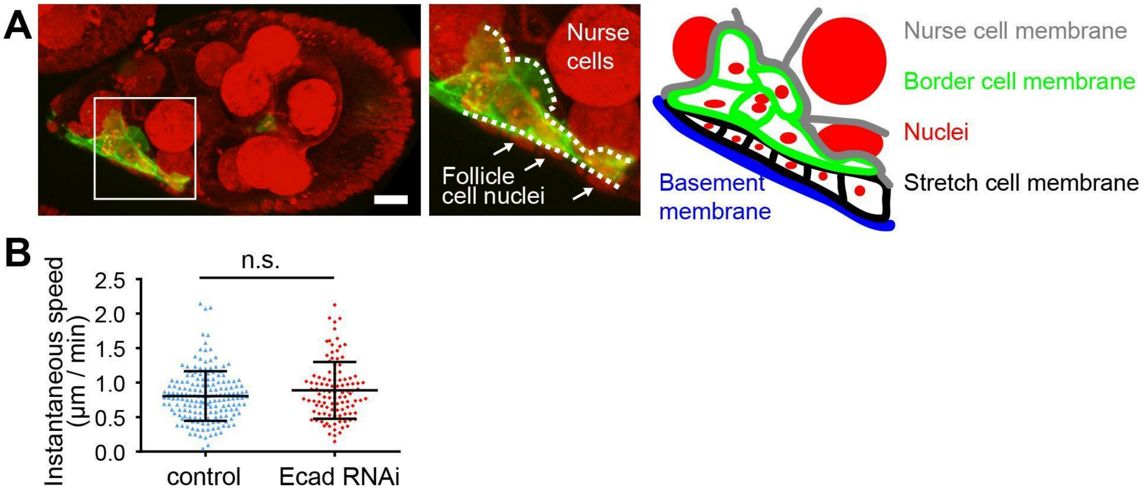

Fig. S5. Effect of nurse cell Ecad knockdown on border cell migration

(A) In nurse cell E-cadherin knockdown, border cells (marked by Slbo-PHEGFP and outlined) migrate in between follicle cells (white arrows) and nurse cells. Scale bars, 20 μm. (B) Quantification of instantaneous migration speed every 4 minutes in control (Matalpha-Gal4>UAS-wRNAi) or Matalpha4-Gal4>UAS-Ecad RNAi. In contrast to RTK inhibition, migration speed was not initially reduced. Data from eight controls n = 178 time points and eight nurse cell Ecad RNAi egg chambers n = 107 time points.

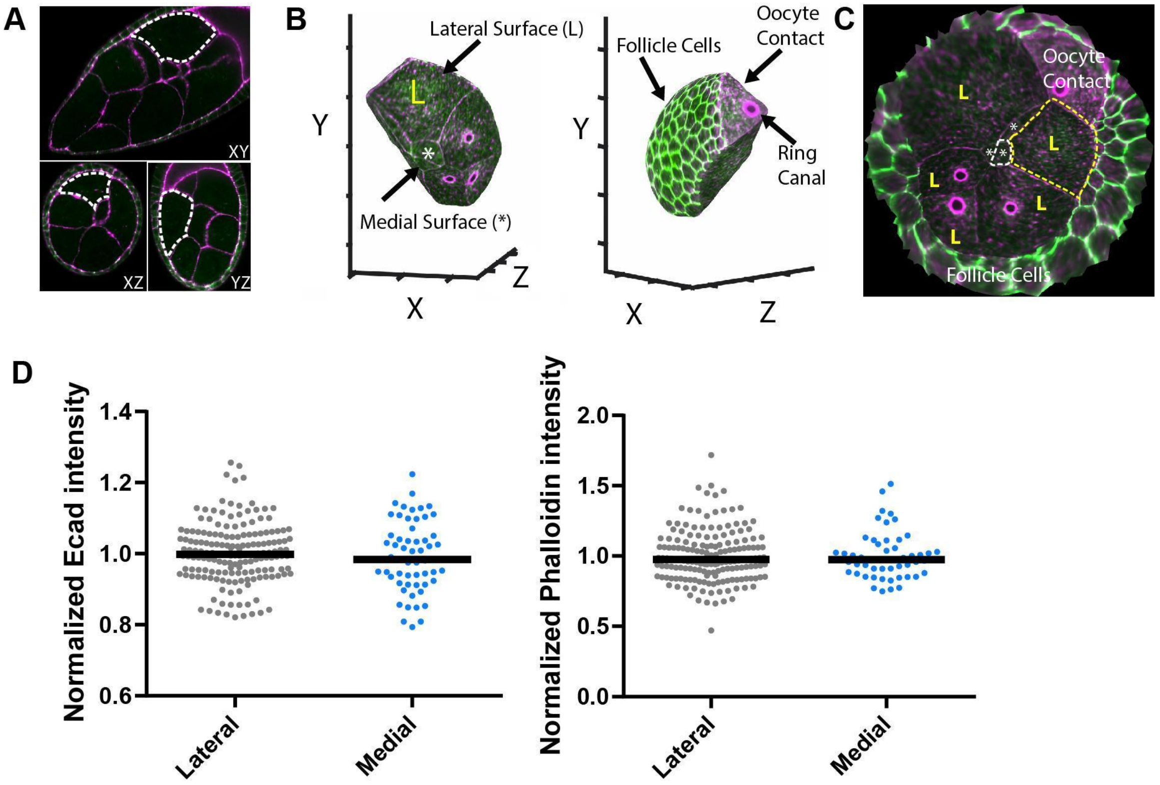

Fig. S6. Isotropic light sheet imaging of E-cadherin on medial and lateral nurse cell surfaces

(A) Near-isotropic light sheet imaging of a stage 9 egg chamber stained for F-actin with phalloidin (magenta), and anti-Ecad antibody (green). Dashed lines indicate the boundaries of a single nurse cell in the XY/XZ/YZ orthogonal views. (B) 3D reconstruction of the surface of the nurse cell outlined in (A). (C) "Pullback" of the surface of the 3D reconstruction in (B) created with the Images Surfaces Analysis Toolkit (*24*). The pullback represents the summed intensity projection of 1.5um thickness around the surface of the 3D object in (B). Medial surfaces are represented by (*) and lateral surfaces by (L). (D) Quantification from four egg chambers of E-cadherin and F-actin (Phalloidin) intensities on medial surfaces vs lateral membranes lacking ring canals. Anova with post-hoc Tukey test and blocking by egg chamber showed no significant difference in E-cadherin (*P* = 0.49) or Phalloidin (*P* = 0.94) intensities.

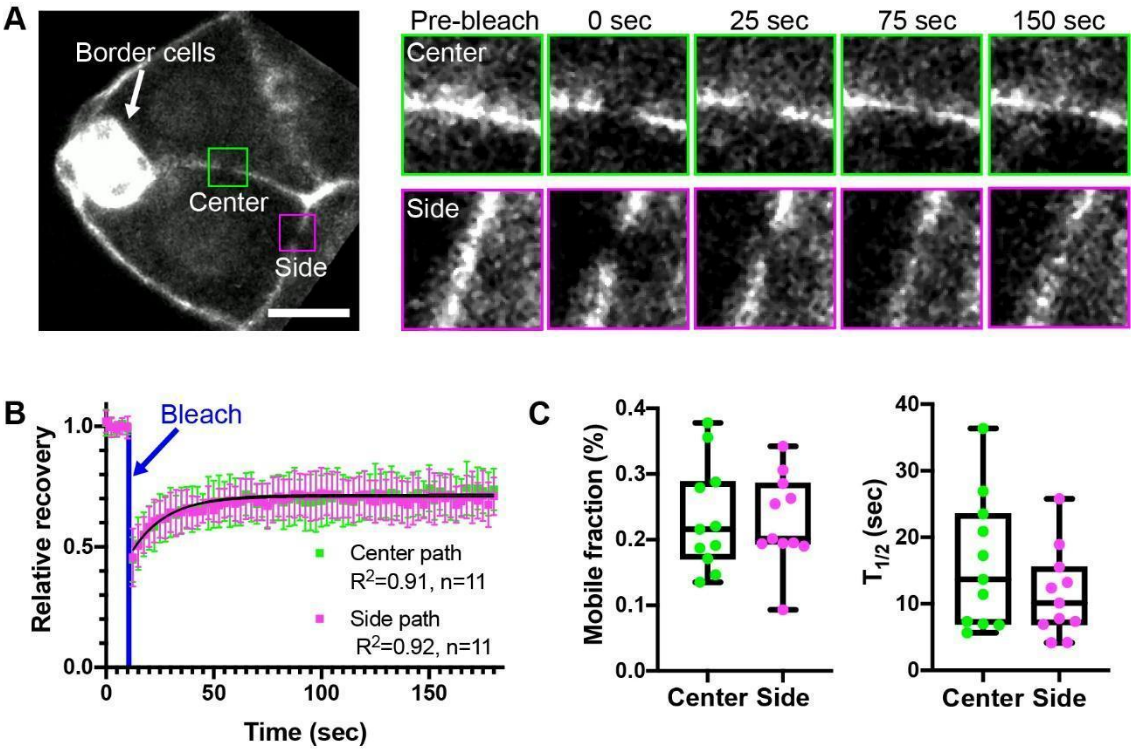

Fig. S7. Fluorescence recovery after photobleaching (FRAP) shows no difference in E-cadherin stability on center and side paths

(A) Stage 9 egg chamber with E-cadherin endogenously tagged with GFP. Insets show center vs. side membrane E-cadherin signal. Scale bar, 20 µm. (B) Quantification of the FRAP experiment shown in (A). (C) Quantification of the mobile fraction and $T_{1/2}$ of E-cadherin on center vs. side membranes.

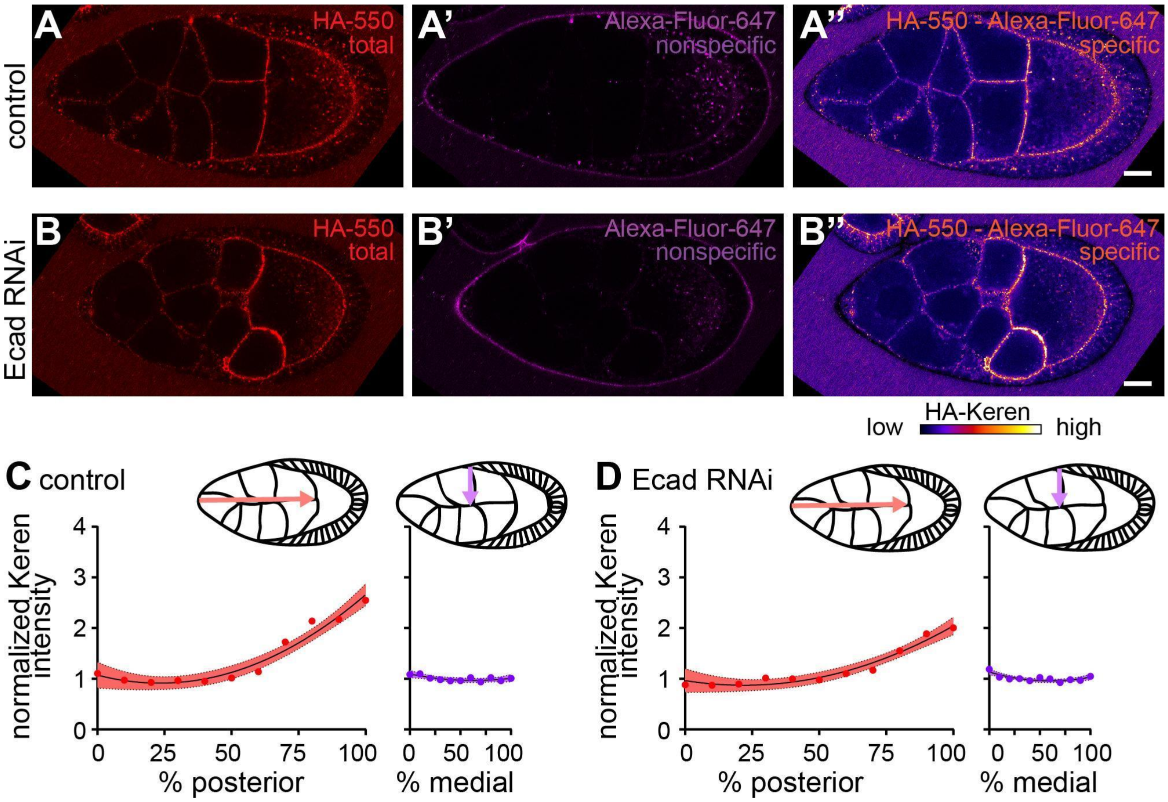

Fig. S8. HA-Krn concentration in control and nurse cell E-cadherin RNAi expressing egg chambers

E-cadherin RNAi does not cause a redistribution of HA-Krn that would account for lateral path selection. (A) Confocal imaging of anti-HA-550 staining of a living stage 9 egg chamber from a heterozygous, CRISPR-tagged, HA-Keren fly (negative control) [genotype: MatalphaGal4/+;HA-Keren/+;UAS-wRNAi/+]. (A') Labeling of the same egg chamber using a non-specific Alexa-647 antibody. (A'') To derive the specific pattern of HA-Krn, the 647 fluorescence intensity was subtracted from the total 550 fluorescence intensity (see methods for details). (B-B'') Staining of a stage 9 egg chamber from MatalphaGal4/+;HA-Keren/+;UAS-EcadRNAi/+ using the same method as in A-A''. (C-D) Quantification of Keren intensity along the anterior-posterior (coral) and lateral-medial (purple) axes. Data points from six egg chambers are shown for each genotype. The line represents the best fit trendline of normalized Keren distribution along the A/P or L/M axis. Shading represents the standard deviation of the best fit trendline. There is no statistically significant difference between control and nurse-cell Ecad RNAi along the mediolateral axis ($P = 0.6$) or the relevant portion of the A/P axis ($P = 0.6$) that border cells encounter in the nurse-cell Ecad RNAi condition (see Fig. 2D). Scale bars, 20 μm.

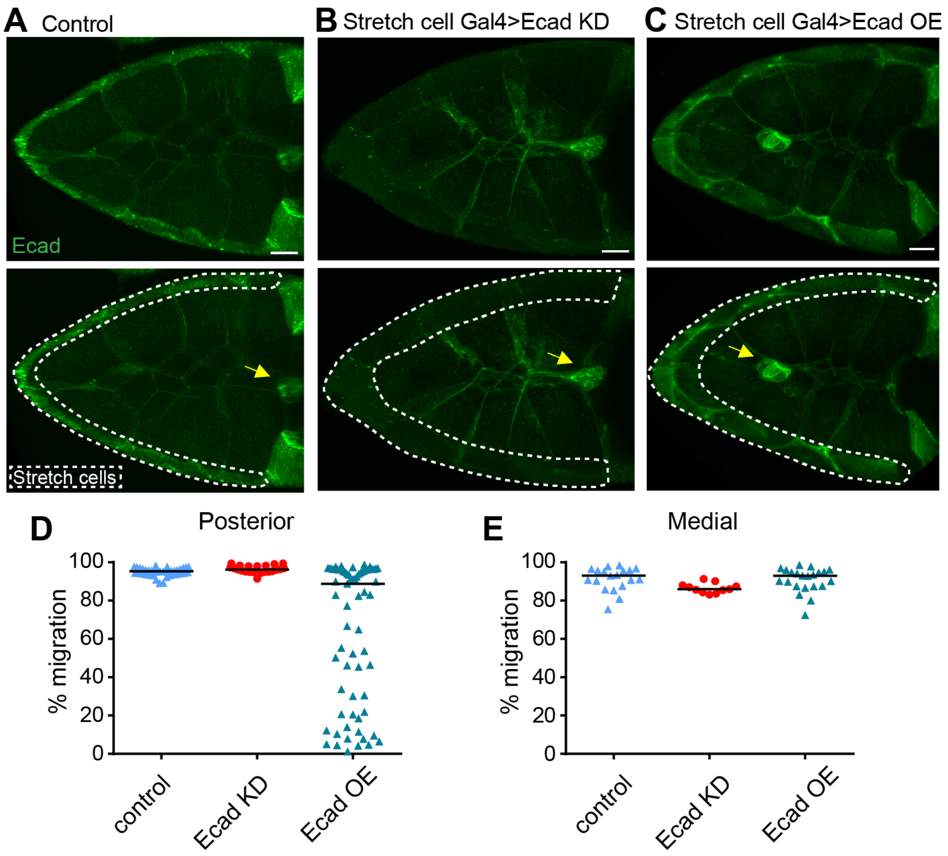

Fig. S9. Stretch cell Ecad knockdown shows no medial guidance defect

Projections of 18 confocal sections (2um each) of anti-E-cadherin staining of early stage 10 egg chambers in the indicated genotypes. (A) control stretch cell Gal4>wRNAi, (B) Decreased Ecad level in stretch cell Gal4>Ecad RNAi. (C) Increased Ecad in stretch cell Gal4>Ecad. Scale bar, 20 µm. Dotted lines show stretch cell regions; Arrows indicate border cell clusters. Quantification of posterior (D) and medial (E) migration in egg chambers for each genotype. Scale bars, 20 µm.

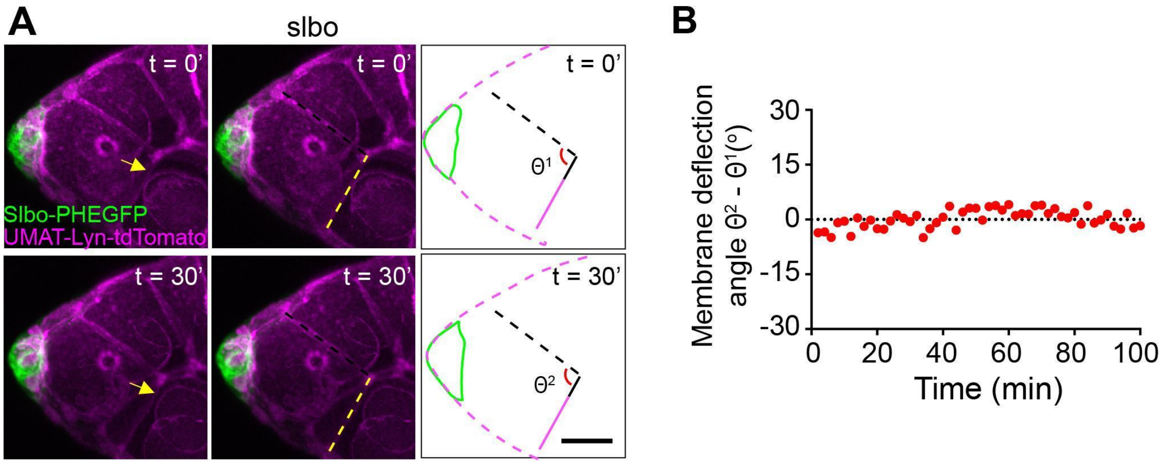

Fig. S10. Nurse cell membrane deflections require border cell migration

(A) Still images from a movie of a *slbo* mutant egg chamber in which border cells do not migrate (*26*). No nurse cell juncture deflection occurs, showing that they are not random fluctuations; rather they are caused by border cells actively pulling. Scale bar, 20 μm. (B) Representative trace of normalized nurse cell membrane deflections in *slbo* mutant.

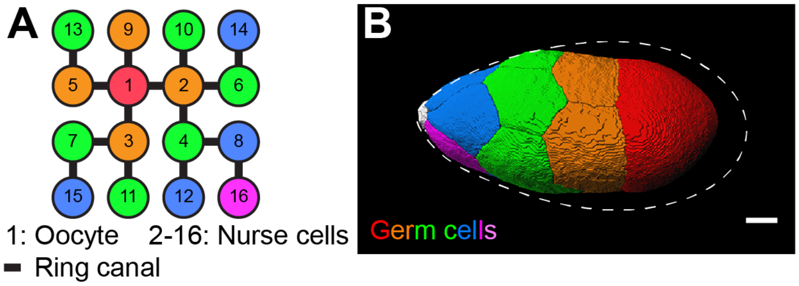

Fig. S11. Nurse cell arrangements in control egg chambers

The 16 germ cells derive from a single germline precursor, which undergoes four rounds of cell division with incomplete cytokinesis. Residual, stabilized cleavage furrows called ring canals thus connect germline cells to one another in a regular pattern. (A) Schematic drawing of the germ cell identity (numbers in circles) based on their birth order and thus ring canal connections (lines) in control egg chambers. Colors indicate distance to the oocyte (#1). (B) 3D reconstruction of germ cell packing in stage 9 egg chambers. White, border cells at the anterior tip. Dashed line indicates the somatic follicle cell layer. Scale bar, 20 µm.

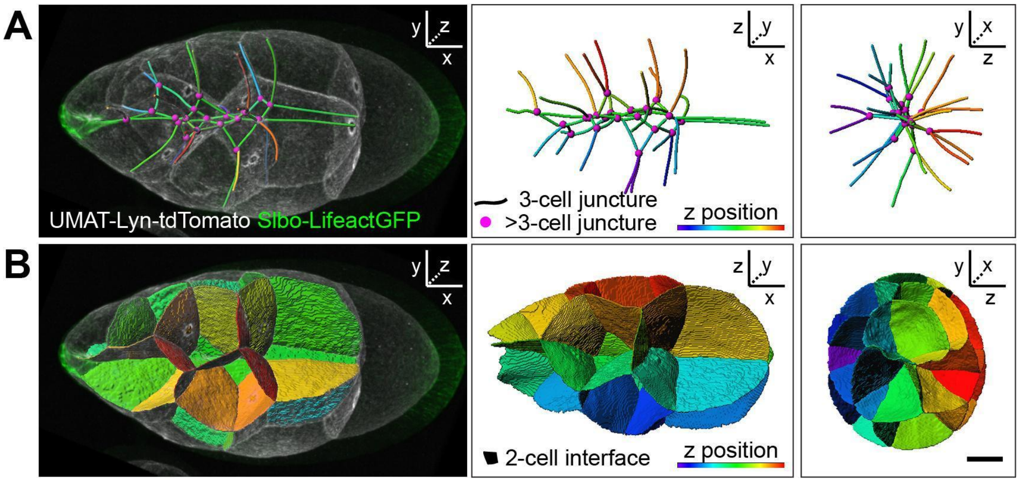

Fig. S12. Three dimensional reconstructions of nurse cell contacts

A second example for Fig.3A and C. (A) 3-nurse cell junctures are represented as lines and color provides position in z. Magenta dots represent junctures of >3 nurse cells. x,y planes (left panels), x,z planes (middle), and y,z planes (right panels) are shown. (B) Two-cell-contacts are shown as surfaces. Scale bar, 20 μm.

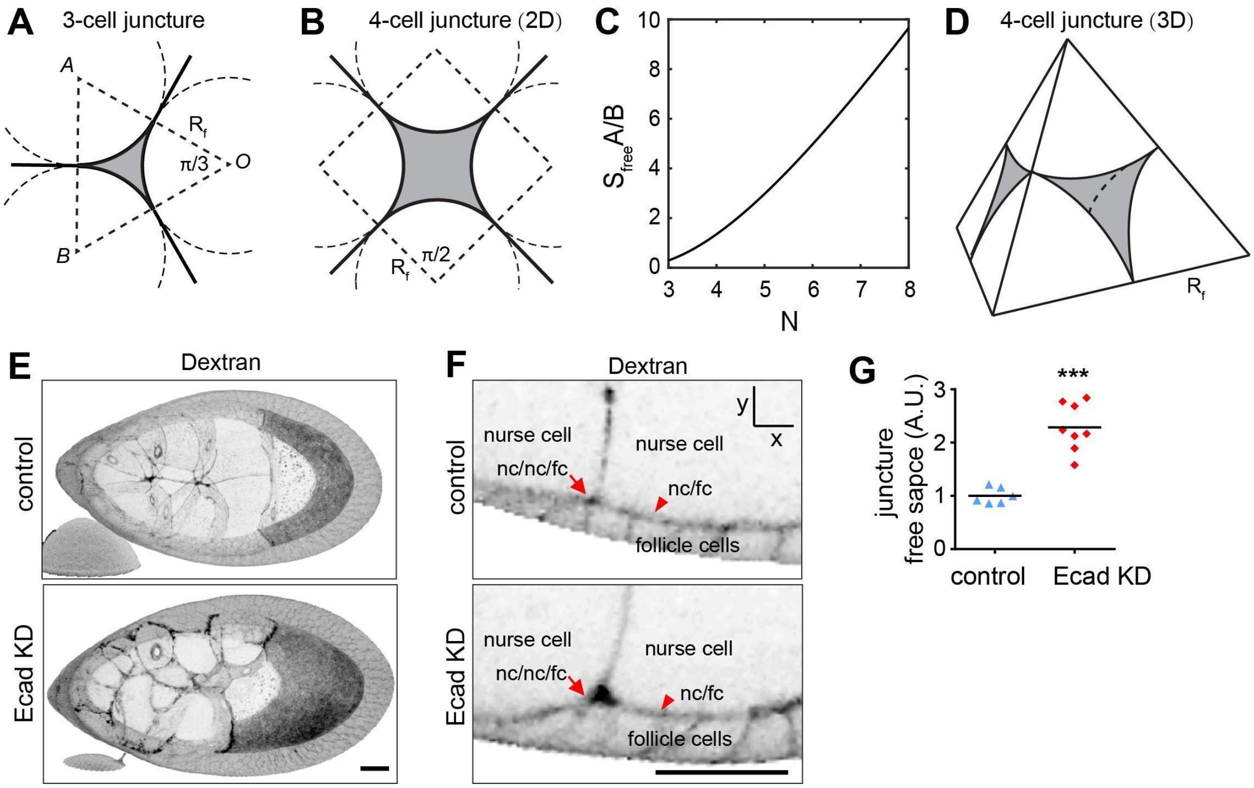

Fig. S13. Geometry of nurse cell junctures and associated free space

(A) The local configuration of 3-cell junctures in a 2D cross section. Nurse cell membranes are represented by solid black lines and R_f is the local radius of the nurse cell. The free space between the nurse cells, shaded gray, is the area of the polygon (OAB), a triangle in this case, minus the area of the circular sector with centers at A, B and O, multiplied by the number of nurse cells in the juncture. (B) The configuration of a 4-cell juncture in 2D. In this case, the polygon is a square. (C) S_{free} is a function of the balance between adhesion (A) energy gained and the cost of bending (B) nurse cell membranes and increases with increasing N at the junctures. Bending energy proved negligible (see ST2) (D) The configuration of a 4-cell juncture in 3D. The nurse cell membrane is represented by spherical surfaces that join together. The centers of the spheres are the vertices of a tetrahedron, which has edges with length $2R_f$. The volume of the free space, again shaded gray, is the volume of the tetrahedron minus the volume of the spherical caps. (E) Dextran filled spaces (black) in a control stage 9 egg chamber or with germline E-cadherin knockdown (KD). (F) Lateral view of dextran showing Ecad knockdown enlarged space. (G) Quantification of 3-cell junctures in 2D. n = 6, 8 pairs of junctions from 3 control and 4 ECad KD egg chambers. Bars show mean. ***, $P < 0.001$ (Mann-Whitney test), A.U. arbitrary unit. Scale bar, 20 µm.

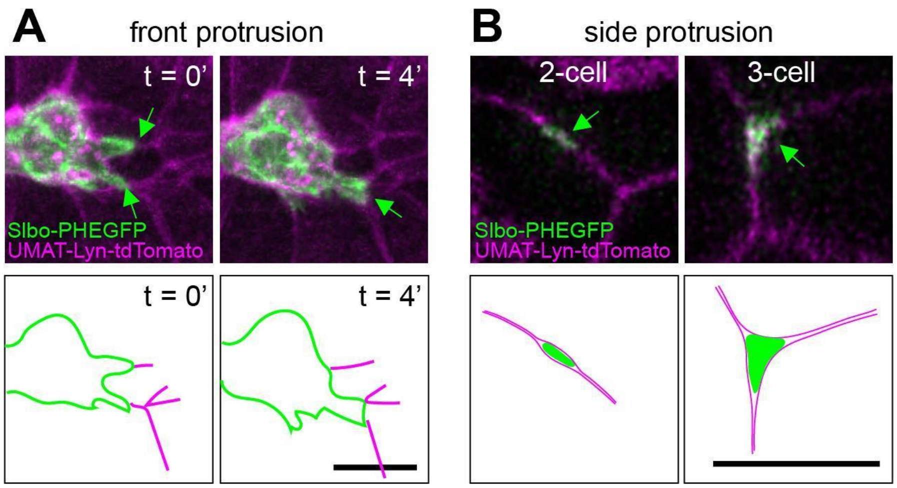

Fig. S14. Border cell protrusions favorite multicellular junctures

(A) Still images from two time points of a 3D movie. Two forward-directed protrusions (green arrows in A) encounter different nurse cell junctions (magenta). The protrusion that reaches a >3 cell junction wins (green arrow in B, n = 11 from 7 movies). (B) Cross-sections showing side protrusions (green) at 2-cell interface or 3-cell junctions (magenta). Scale bars, 20 μm.

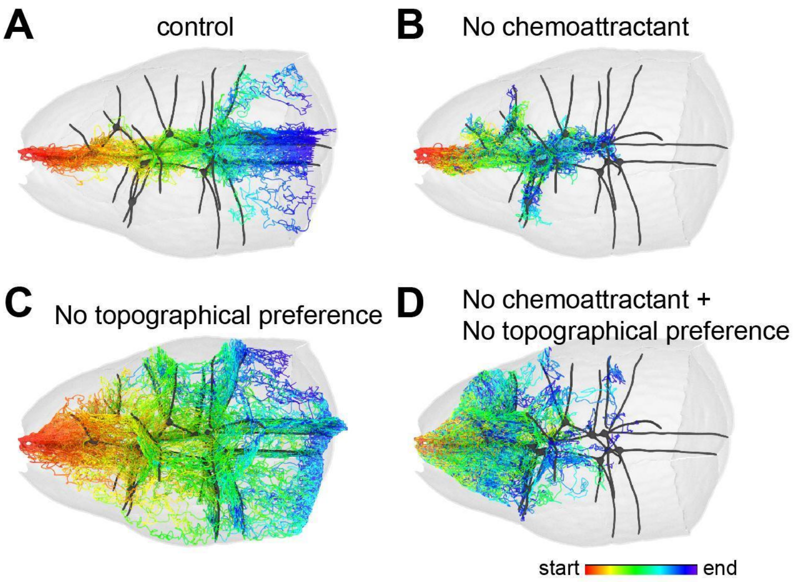

Fig. S15. Plots of 99 simulated migration paths

Rainbow display of 99 simulated migration paths (red=start and blue=end) for each of the indicated conditions. (A) Normal condition in which path selection is a function of both a posterior chemoattractant gradient and increasing preference for junctures with increasing numbers of nurse cells. At the end of migration the influence of geometry weakens, correlating with loss of >3 nurse cell junctures. (B) Removal of the posterior chemoattractant gradient causes 100% posterior migration defect and 10% medial migration defect. Those clusters that deviate from the central path migrate into side paths with >3-cell junctures. (C) In the presence of chemoattractant but absence of preference for multiple nurse cell junctures, clusters migrate posteriorly but are distributed essentially randomly with respect to the mediolateral axis. (D) In the absence of either chemoattractant or junctional preference, clusters exhibit both posterior and medial migration defects.

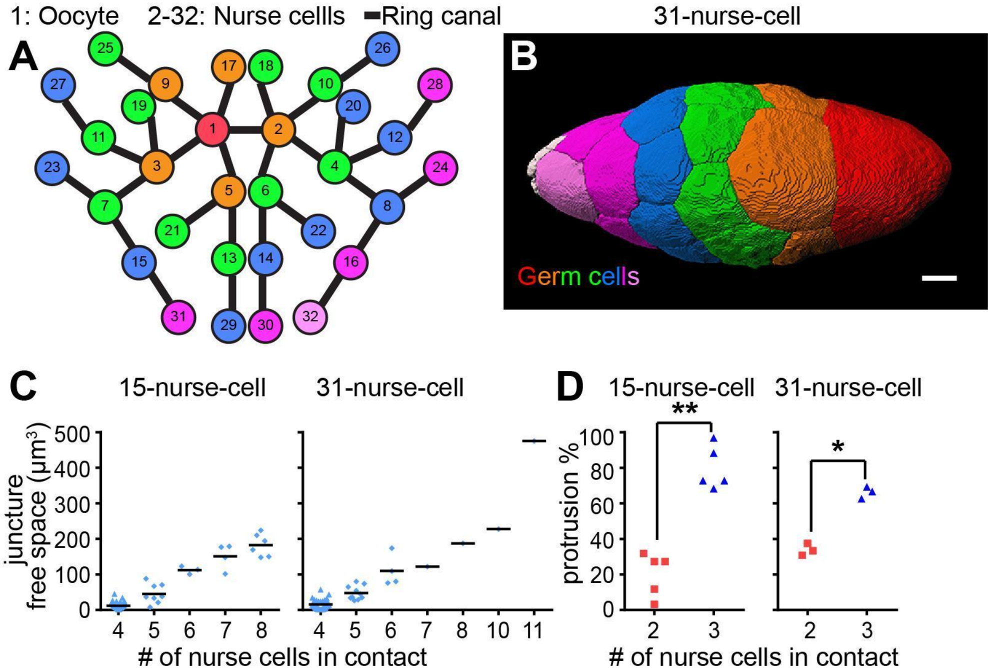

Fig. S16. Nurse cell arrangements in mutants with increased number of nurse cells

(A) Schematic of the pattern of ring canal (lines) connections between individual germ cells (numbers in circles) in a 31-nurse-cell egg chamber. (B) 3D reconstruction of germ cell packing in a 31-nurse-cell stage 9 egg chamber. Germ cells are color coded according to ring canal number, which also correlates with proximity to the oocyte (red cell, #1). Border cells are at the anterior tip in B and are pseudocolored in white. Scale bar, 20 µm. (C) Quantification of extracellular spaces filled with fluorescent dextran in control and 31-nurse-cell egg chambers (n = 7, 3 egg chamber). (D) Quantification of side protrusion preferences as a fraction of total protrusions in control (n=5) and 31-nurse-cell (n=3) movies. **, $P < 0.01$, *, $P < 0.05$ (paired t test). Neither intercellular spaces nor protrusion preference for 3-nurse-cell junctures was altered in 31-nurse-cell egg chambers.

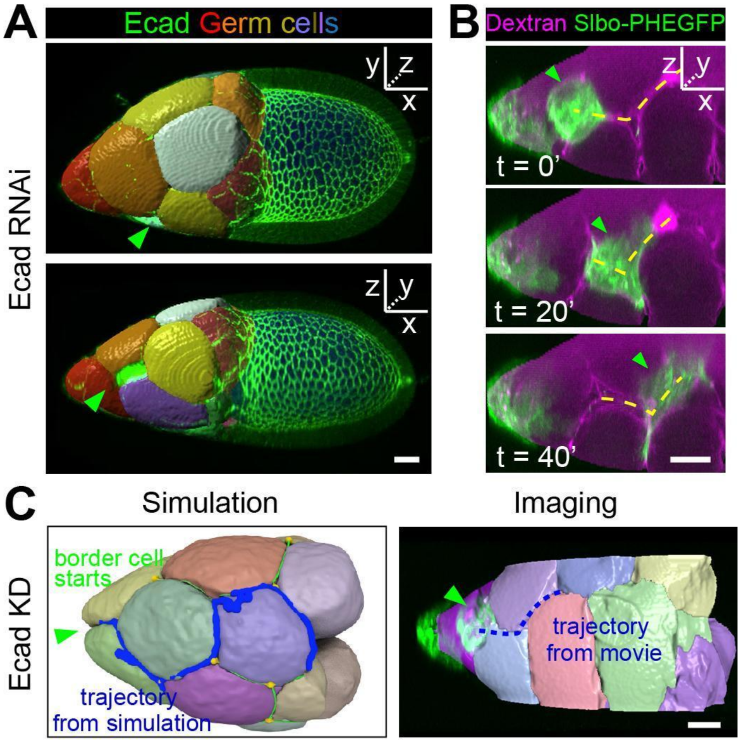

Fig. S17. Border cells prefer multiple cell junctures in egg chambers with reduced germline Ecad

(A) Three dimensional reconstructions of nurse cells in a fixed egg chamber with germline Ecad RNAi showing border cells in nurse cell/nurse cell/follicle cell grooves. (B) Still images from a movie showing border cells (green arrowhead) zig zagging(dashed yellow lines) along grooves. Yellow dashed line indicates the nurse cell junctions that the border cells migrate along. Green arrowhead points to the border cells. (C) 3D reconstructions of nurse cells with Ecad knockdown showing border cells in nurse cell-nurse cell-follicle cell grooves. Scale bars, 20 μm.

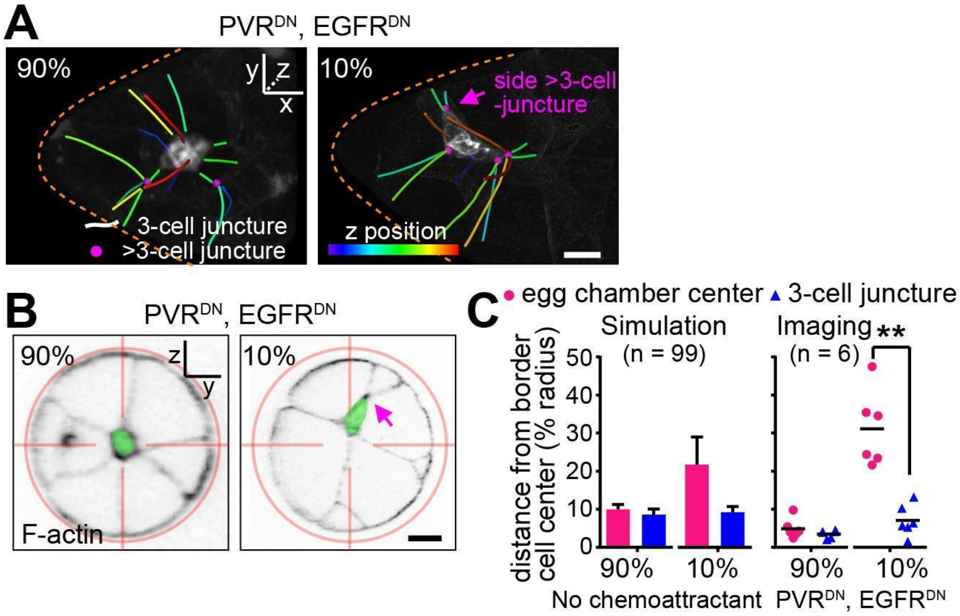

Fig. S18. Border cells prefer multiple cell junctures in PVR^{DN}, EGFR^{DN} egg chambers with off-center border cells

(A and B) Border cell cluster location relative to nearby ≥3-cell junctures in representative egg chambers in which border cells express PVR^{DN} and EGFR^{DN}. In 90% of egg-chambers, border cell clusters remain in the center, while 10% migrate off-center (Fig. 1F, right panel). (C) Quantification of distance from border cell centroid to the egg chamber center and the nearest 3-cell juncture. Simulation of no chemoattractant is done by removing the chemoattractant term. **, *P* < 0.01 (paired t-test). Scale bars, 20 μm.

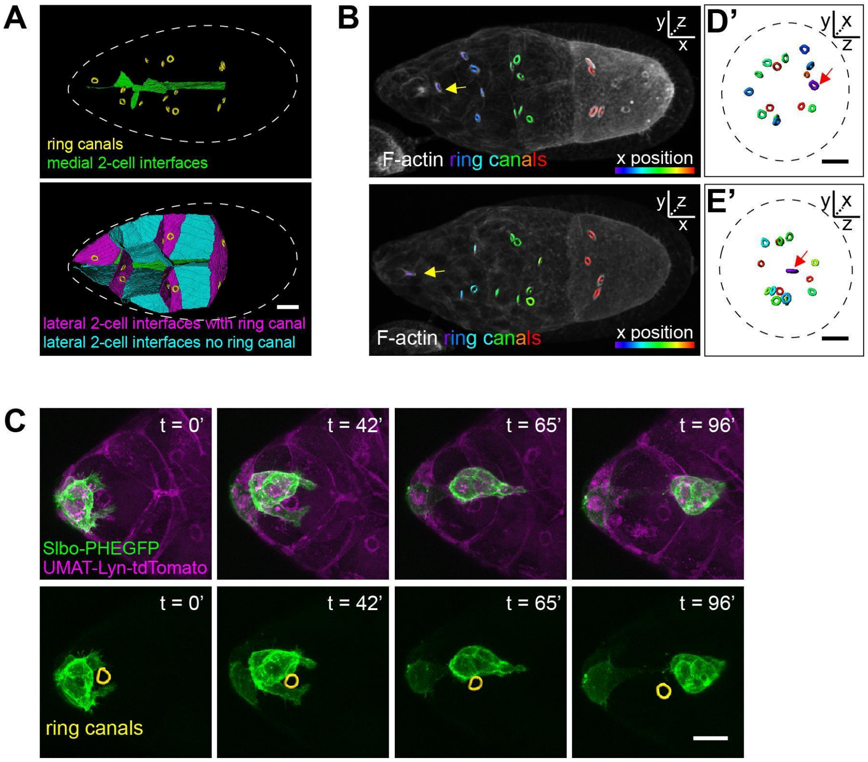

Fig. S19. Ring canals are neither necessary nor sufficient to steer border cells

(A) Ring canal locations on 2-germ cell interfaces. Medial interfaces (green) are free of ring canals (left panel). 15 lateral cell interfaces contain ring canals (magenta, right panel) and 26 do not (cyan). (B) Lateral and anterior 3D projection views of reconstructed 3D ring canals (colored circles) in early stage 9 egg chambers in which ring canals are absent (upper right panel) or present (lower right panel) in the central path. (D) Still images from a time lapse movie showing border cells migrating past a ring canal. Dashed line outlines the egg chamber. Scale bars, 20 µm.

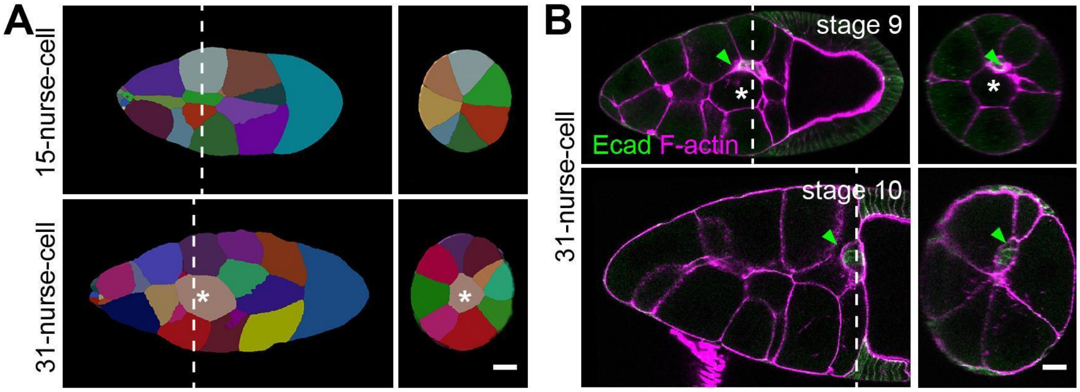

Fig. S20. A centrally located nurse cell does not block border cell migration

(A) Reconstructed nurse cell arrangements showing all nurse cells contact follicle cells in control, but there are 1-2 nurse cells in the center in 31-nurse-cell egg chambers. (B) Border cells migrate around a central nurse cell in stage 9 (n=9) and reach the oocyte border by stage 10 in an egg chamber with 31 nurse cells (n=19). White lines indicate cross-sectional planes shown in the right panels. Green arrowhead points to the border cells. White asterisks indicate the central nurse cell. Scale bars, 20 μm. Although the central path normally is free of cells, the presence of a central nurse cell does not block migration.

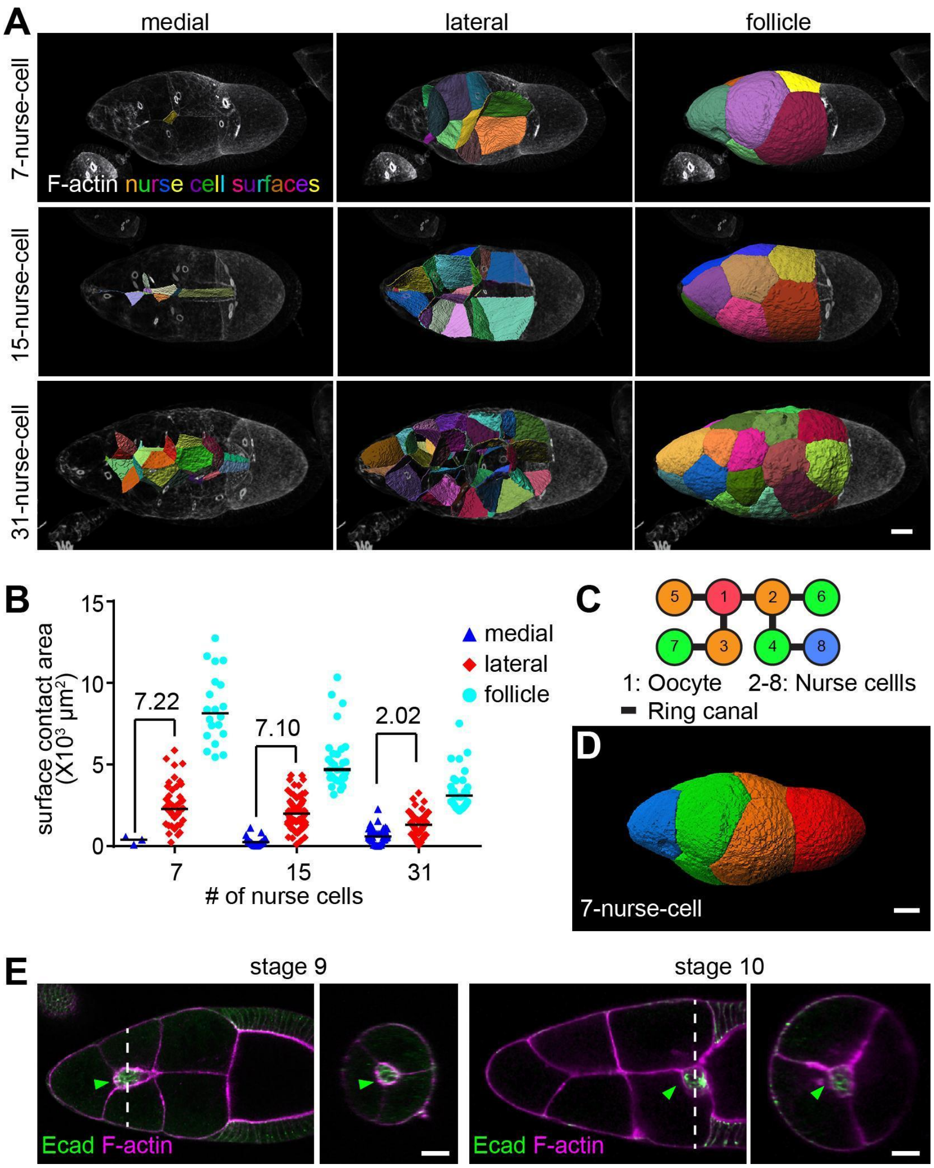

Fig. S21. The ratio of medial to lateral surface areas is not critical for border cell migration

(A) Lateral view of segmented 3D nurse cell surface-surface contacts in early stage 9 egg chambers. (B) Quantification of the areas of different types of nurse cell surface contacts. Each dot represents the area of the contact between a single nurse cell and a neighboring nurse cell or follicle cells. Numbers indicate the mean value normalized to that of the medial path in each genotype to compare relative differences between medial and lateral surface areas. Data from $n = 3, 2, 1$ early stage 9 egg chambers. Absolute size of medial surfaces: 15NC (mean ± SD = 286 ± 256) and 31NC (mean ± SD = 658 ± 462) are significantly different ($P < 0.0001$, unpaired t test). 15NC and 7NC (mean ± SD = 347 ± 247) are not significantly different. Note there is only 1 medial surface in each 7NC egg chamber. (C) Schematic drawing of the pattern of ring canal (lines) connections between individual germ cells (numbers in circles) in a 7-nurse-cell egg chamber. (D) 3D reconstruction of germ cell packing in a 7-nurse-cell early stage 9 egg chambers. Germ cells are color coded according to ring canal number, which also correlates with proximity to the oocyte (red cell, #1). (E) Border cells migrated along the multiple cell juncture and reached the oocyte border in stage 10 egg chambers with 7 nurse cells (n=41). White dashed lines indicate cross sectional plane shown in the right panel. Green arrowhead points to the border cells. Scale bars, 20 μm.

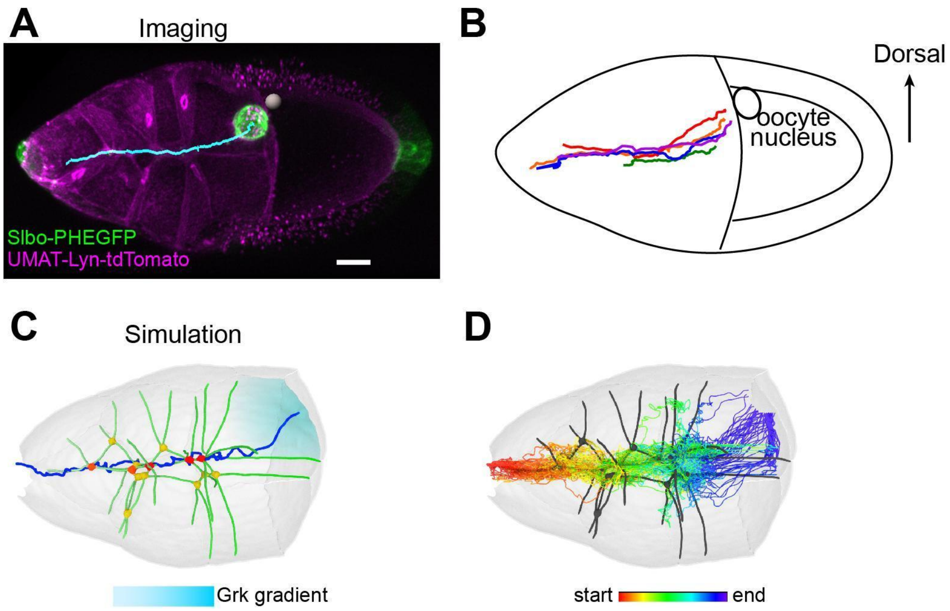

Fig. S22. Dosal migration with Grk gradient

(A) Live imaging showing dorsal migration near the oocyte. The cyan line indicates the track taken by border cells in a movie (movie S2). White sphere indicates location of the oocyte nucleus. Scale bar, 20 μm. (B) Tracking dorsal migration in live movies aligned according to the oocyte nucleus location by rotation around the x-y plane. Colors indicate trajectories from 5 different egg chambers. (C) Representative simulation of a border cell migration path when the Grk gradient (cyan shading) is included (movie S3). Note that between the most posterior four nurse cells, >3-cell junctures (colored dots) are absent, weakening the geometry cue and allowing the chemical cue to lead cells through a suboptimal physical space. (D) 99 simulations with Grk gradient.

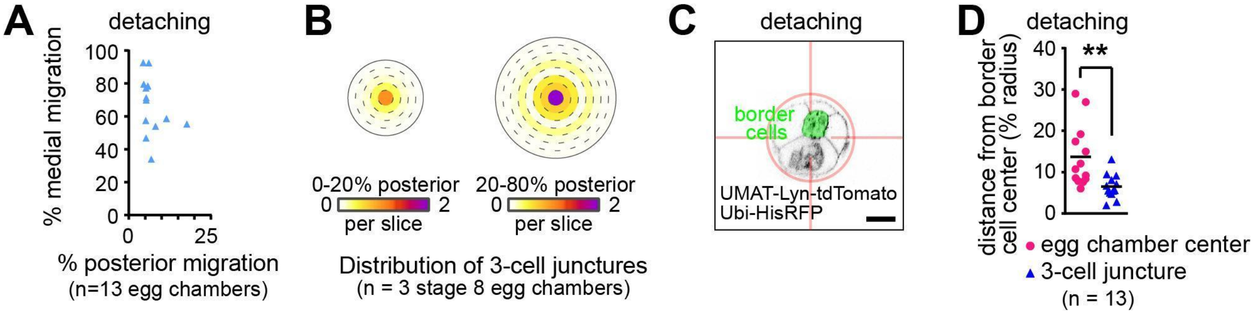

Fig. S23. Border cell position when delaminating from anterior follicle cells

(A) Migration in control stage 9 egg chambers when border cells are detaching from anterior follicle cells. (B) Heat map showing distributions of 3-cell junctures as a function of mediolateral position in stage 8 egg chambers at 0-20% posterior location (left) or 20-80% posterior location (right). (C) Cross-sections showing border cells (green pseudocolor) and nurse cell junctions (black lines) relative to the egg chamber center. Scale bar, 20 µm. (D) Comparison of the distance from the border cell centroid to the egg chamber center (pink dots) vs the nearest 3-cell junction (blue triangles) in 13 early stage 9 egg chambers when border cells are detaching from anterior follicle cells. **, *P* < 0.01 (paired t-test).

Supplementary Tables

Table S1. List of fly stains used in this study

	Purpose	Genotype	Source	Reference
Fluorescent markers	border cell membrane marker	slbo-4XPHEGFP (III)	Hsin-Ho Sung	
		slbo-LifeactGFP	lab stock	
	nurse cell membrane marker	UMAT-Lyn-tdTomato (II) and (III)	Hsin-Ho Sung	(*27*)
	all cell nuclei marker	ubi-HisRFP	Hsin-Ho Sung	
	Ecad marker	y,w; shgGFP	BDSC 60584	
CRISPR KI	inject PVF1N1	w;vas-Cas9 (III)	BestGene 51324	
	inject PVF1N2, PVF1C, and KerenC	yw; nos-Cas9 (II-attp40)	BestGene	
	inject KerenN	y, vas-Cas9, w	BestGene 55821	
	inject SpitzN and SpitzC	yw; nos-Cas9 (III-attp2)	BestGene	
	remove scarless in KerenN, KerenC	w; 3XP3-ECFP, tub-PBac; MKRS/TM6B	BDSC 32070	
	remove scarless in PVF1N1, PVF1N2, PVF1C, SpitzN, and SpitzC	w; CyO, w+, tub-PBac/wg	BDSC 8283	
Gal4 drivers	border cell Gal4 driver	w; slbo-Gal4 (II)	lab stock	
		Gal80ts; Fruitless-Gal4/TM6B	lab stock	
		109C1-Gal4	BDSC 7020	
	somatic cell mosaic driver	hsFlp; Ay-Gal4, UAS-GFP	lab stock	
	stretch cell Gal4	w; c329b-Gal4/TM3	BDSC 3746	
	nurse cell Gal4	w; matalpha4-Gal4 (II)	BDSC 7062	
		nos-Gal4/CyO; bam-Gal80/TM6	Huynh Jean Rene	(*21*)
		Gal4::VP16	BDSC 64277	
UAS transgenes	PVR, EGFR inhibition	UAS-PVR[DN]; UAS-EGFR[DN]	lab stock	
		UAS-EGFR-RNAi/CyO; UAS-PVR-RNAi/TM6	lab stock	
	PVF1 overexpression	UAS-pvf1; UAS-pvf1/TM6B,Hu	lab stock	
	Ecad overexpression	UASp-EcadFL	lab stock	
		UAS-EcadGFP	lab stock	
RNAi	Ecad RNAi	shgRNAi (HMS00693)	BDSC 32904	(*17*)
		shgRNAi2 (V103962)	VDRC 103962	(*17*)
	shrub RNAi	shrubRNAi (HMS01767)	BDSC 38305	(*21*)
	cycE RNAi	cycERNAi (HMS00060)	BDSC 33654	(*28*)
	wRNAi	wRNAi	lab stock	
mutant	slbo	slbo[e7b]	lab stock	
		slbo[PZ01310]	lab stock	

Table S2. List of fly genotypes in each experiment

Figure	Panel	Group	Genotype
1	A-B	WT	w; slbo-4XPHEGFP, UMAT-Lyn-tdTomato/+
	D-E	HA-Keren	y,w/w; HA-Keren[N1]
	F	control	w; slbo-Gal4/+
		PVR[DN], EGFR[DN]	w; UAS-PVR[DN]/slbo-Gal4; UAS-EGFR[DN]/+
	G-H	control clone	hsFlp/w; Ay-Gal4, UAS-GFP/+; ubi-HisRFP, slbo-4XPHEGFP, UMAT-Lyn-tdTomato/+
		PVF overexpression in clone	hsFlp/UAS-pvf1; Ay-Gal4, UAS-GFP/+; ubi-HisRFP, slbo-4XPHEGFP, UMAT-Lyn-tdTomato/UAS-pvf1
2	A-D	control	w; matalpha4-Gal4/+
		Ecad RNAi	w/y,sc,v, sev; matalpha4-Gal4/+; shgRNAi (HMS00693)/+
		Ecad overexpression	w; matalpha4-Gal4/UASp-EcadFL
	E-H	control	w; ubi-HisRFP, slbo-4XPHEGFP, UMAT-Lyn-tdTomato/+
		Ecad RNAi	matalpha4-Gal4/+; shgRNAi (HMS00693)/ubi-HisRFP, slbo-4XPHEGFP, UMAT-Lyn-tdTomato
3	A-D	WT	w; slbo-GaL4/UAS-LifeactGFP
	E	WT	w; UMAT-Lyn-tdTomato/+; UAS-HisRFP/slbo-LifeactGFP
	F-G	WT	w; matalpha4-Gal4/+
	H	WT	w; ubi-HisRFP, slbo-4XPHEGFP, UMAT-Lyn-tdTomato/+
4	C, E	control	w; slbo-Gal4/+
		31-NC	w/y,v; nos-Gal4/shrubRNAi; bam-Gal80/+

Table S3. List of fly genotypes in each supplementary experiment

Figure	Panel	Group	Genotype
S1	A-B	WT	w; slbo-4XPHEGFP, UMAT-Lyn-tdTomato/+
	C	WT	w; slbo-Gal4/+
S2	A	HA-Keren	y,w/w; HA-Keren[N1]
	B	WT	w1118
	C-D	HA-PVF1	HA-PVF1[N2]
S3	A	PVR[DN], EGFR[DN]	w; UAS-PVR[DN]/slbo-Gal4; UAS-EGFR[DN]/+
	B	control	w; slbo-Gal4/+; ubi-HisRFP, slbo-4XPHEGFP, UMA-TLyn-tdTomato/+
		PVR[DN], EGFR[DN]	w; UAS-PVR[DN]/slbo-Gal4; UAS-EGFR[DN]/ubi-HisRFP, slbo-4XPHEGFP, UMAT-Lyn-tdTomato
	C	Slbo-control	w; slbo-Gal4/+
		Slbo-DN	w; UAS-PVR[DN]/slbo-Gal4; UAS-EGFR[DN]/+
		Slbo-RNAi	w; UAS-EGFR-RNAi/slbo-Gal4; UAS-PVR-RNAi/+
		Fruitless-control	w; Gal80ts; Fruitless-Gal4/TM6B
		Fruitless-DN	w; Gal80ts/UAS-PVR[DN]; Fruitless-Gal4/UAS-EGFR[DN]
		Fruitless-RNAi	w; Gal80ts/UAS-EGFR-RNAi; Fruitless-Gal4/UAS-PVR-RNAi
		109C1-control	w;109C1-Gal4/+
		109C1-DN	109C1-Gal4; UAS-PVR[DN]/+; UAS-EGFR[DN]/+
		109C1-RNAi	109C1-Gal4; UAS-EGFR-RNAi/+; UAS-PVR-RNAi/+
S4	A-C	PVF OE in clone	hsFlp/UAS-pvf1; AyGal4,UAS-GFP/+; ubiHisRFP, slbo4XPHEGFP, UMATLynTdTom/UAS-pvf1
	D	PVF overexpression in stretch cells	UAS-Pvf1/+; slbo-LifeactGFP/+; c329b-Gal4/UAS-LifeactRFP
S5	A	Ecad RNAi	matalpha4-Gal4/wRNAi; shgRNAi (HMS00693)/ubi-HisRFP, slbo-4XPHEGFP, UMA-TLyn-tdTomato
	B	control	matalpha4-Gal4/+; ubi-HisRFP, slbo-4XPHEGFP, UMA-TLyn-tdTomato/+
		Ecad RNAi	matalpha4-Gal4; shgRNAi (HMS00693)/ubi-HisRFP, slbo-4XPHEGFP, UMA-TLyn-tdTomato
S6	A-D	WT	W1118
S7	A-C	WT	y,w; shgGFP
S8	A-D	control	matalpha4-Gal4/+;HA-Keren[N1]/+
		Ecad RNAi	matalpha4-Gal4/+;HA-Keren[N1]/shgRNAi (HMS00693)
S9	A-E	control	shgRNAi2 (V103962)/+
		Ecad RNAi	shgRNAi2 (V103962)/+; c329b-Gal4/+
		Ecad OE	c329b-Gal4/UAS-EcadGFP
S10	A-B	slbo mutant	slbo[e7b]/slbo[PZ01310]; ubi-HisRFP, slbo-4XPHEGFP, UMAT-Lyn-tdTomato/+
S11	B	WT	w; slbo-GaL4/UAS-LifeactGFP
S12	A-B	WT	w; UMAT-Lyn-tdTomato/+; UAS-HisRFP/slbo-LifeactGFP
S13	E-G	WT	w; matalpha4-Gal4/+
		Ecad RNAi	w/y,sc,v, sev; matalpha4-Gal4/+; shgRNAi (HMS00693)/+

S14	A-B	WT	w; ubi-HisRFP, slbo-4XPHEGFP, UMAT-Lyn-tdTomato/+
S16	B-C	control	w; matalpha4-Gal4/+
		31-NC	nos-Gal4/shrubRNAi; bam-Gal80/ubi-HisRFP, slbo-4XPHEGFP, UMAT-Lyn-tdTomato
	D	control	w; ubi-HisRFP, slbo-4XPHEGFP, UMAT-Lyn-tdTomato/+
		31-NC	nos-Gal4/shrubRNAi; bam-Gal80/ubi-HisRFP, slbo-4XPHEGFP, UMAT-Lyn-tdTomato
S17	A	Ecad RNAi	w/y,sc,v, sev; matalpha4-Gal4/+; shgRNAi (HMS00693)/+
	B-C	Ecad RNAi	matalpha4-Gal4/+; shgRNAi (HMS00693)/ubi-HisRFP, slbo-4XPHEGFP, UMAT-Lyn-tdTomato
S18	A-B	PVR[DN], EGFR[DN]	w; UAS-PVR[DN]/slbo-Gal4, UAS-LifeactGFP; UAS-EGFR[DN]/+
	C	PVR[DN], EGFR[DN]	w; UAS-PVR[DN]/slbo-Gal4; UAS-EGFR[DN]/+
S19	A-B	WT	w; slbo-GaL4/UAS-LifeactGFP
	C	WT	w; ubi-HisRFP, slbo-4XPHEGFP, UMAT-Lyn-tdTomato/+
S20	A-B	15-NC	w; UMAT-Lyn-tdTomato/+; UAS-HisRFP/slbo-LifeactGFP
		31-NC	w/y,v; nos-Gal4/shrubRNAi; bam-Gal80/+
S21	A-B	7-NC	cycERNAi/Gal4::VP16
		15-NC	w; slbo-GaL4/UAS-LifeactGFP
		31-NC	w/y,v; nos-Gal4/shrubRNAi; bam-Gal80/+
	D-E	7-NC	cycERNAi/Gal4::VP16
S22	A-B	WT	w; UMAT-Lyn-tdTomato/+; UAS-HisRFP//slbo-4XPHEGFP
S23	A-B	WT	w; ubi-HisRFP, slbo-4XPHEGFP, UMAT-Lyn-tdTomato/+

Table S4. Predicted mature peptide and cleavage sites

Gene	Protein ID	N-terminal aa after cleavage before mature peptide	Mature peptide	C-terminal aa after cleavage after mature peptide
Keren	NP_524129.1	IFA	CPPTYVAWYCLNDGTCFTVKIHNEILYNCECALGFMGPRC	EYKEI
Spitz	NP_599118.2	TYK	CPETFDAWYCLNDAHCFAVKIADLPVYSCECAIGFMGQRC	EYKE
Pvf1	NP_523407	VRNATP for N1 and ATP for N2	ASCSPQPTIVELKPPAEDEANYYYMPACTRISRCNGCCGSTLISCQPTEVEQVQLRVRKVDRAATSGRRPFTIITVEQHTQCRC	

Inserted 2xHA sequence flanked by linkers:
QFALGGSGGSGGSGGSMYPYDVPDYAGYPYDVPDYAIKAGGSGGSGGSGGSKGEL

Table S5. CRISPR target sites

Keren N	TGGACAGGCGAAGATCGGGA
Keren C	AGCATCACACGGTTCCTGGT
Spitz N	GGGAATGTAATATTGGGCCT
Spitz C	AACATCGGACGCGGCCTCTT
Pvf1 N	GTTGCATTCCTCACGGTTGC
Pvf1 C	CCGCTGCGATTGCCGCACGA

Table S6. Primers for cloning CRISPR target into the pU6-BbsI-chiRNA vector

Keren N gF	CTTCGTGGACAGGCGAAGATCGGGA
Keren N gR	AAACTCCCGATCTTCGCCTGTCCAC
Keren C gF	CTTCGAGCATCACACGGTTCCTGGT
Keren C gR	AAACACCAGGAACCGTGTGATGCTC
Spitz N gF	CTTCGGGAATGTAATATTGGGCCT
Spitz N gR	AAACAGGCCCAATATTACATTCCC
Spitz C gF	CTTCGAACATCGGACGCGGCCTCTT
Spitz C gR	AAACAAGAGGCCGCGTCCGATGTTC
Pvf1 N gF	CTTCGTTGCATTCCTCACCGTTGC
Pvf1 N gR	AAACGCAACGGTGAGGAATGCAAC
Pvf1 C gF	CTTCGCCGCTGCGATTGCCGCACGA
Pvf1 C gR	AAACTCGTGCGGCAATCGCAGCGGC

Table S7. Primers for cloning left and right recombination arm into the pHD-2xHA-ScarlessDsRed vector.

Keren N1 LF	TAGCGGCCGCGAATTAAGTTGGCATGACTAGCGTTTATTG
Keren N1 LR	CACCAAGGGCGAATTGCGGGAAGGTGACATTCGG
Keren N1 RF	TTCCAAGGGCGAATTAATCTTCGCCTGTCCACCGAC
Keren N1 RR	AGGTTTAAACGAATTCAGCCTAAGGTGACGTCTCAG
Keren C1 LF	TAGCGGCCGCGAATTGATCACAACTAAGGCGAGC
Keren C1 LR	CACCAAGGGCGAATTGAATCTCCTTGTACTCGCACC
Keren C1 RF	TTCCAAGGGCGAATTAGATGGCTCGTACCTGCCAACTCGCAACCGTGTGATG
Keren C1 RR	AGGTTTAAACGAATTAGCACTGAAGTCCGCCTT
Spitz N1 LF	TAGCGGCCGCGAATTCGGAAAATAAACGCGGCTAACAG
Spitz N1 LR	CACCAAGGGCGAATTGGGGGAATGTAATATTCGGGCGGGGCGTGGTC
Spitz N1 RF	TTCCAAGGGCGAATTAACATACAAATGTCCGGAAACCT
Spitz N1 RR	AGGTTTAAACGAATTTTGGGTAGCATGCATCATTTT
Spitz C1 LF	TAGCGGCCGCGAATTAAATGGCTCAACTGGTGGACTG
Spitz C1 LR	CACCAAGGGCGAATTGGATCTCCTTGTATTCGCATCGC
Spitz C1 RF	TTCCAAGGGCGAATTAGACAATACTTACCTGCCCAAACGTCCGCGTCCGA
Spitz C1 RR	AGGTTTAAACGAATTCCACCCTTTTGATTGATTTGATTTG
Pvf1 N1 LF	TAGCGGCCGCGAATTTCGTGGTAAACATACGTTTTGAG
Pvf1 N1 LR	CACCAAGGGCGAATTGGGTTGCTGGAGATTGGG
Pvf1 N1 RF	TTCCAAGGGCGAATTAGTGAGGAATGCAACGCCG
Pvf1 N1 RR	AGGTTTAAACGAATTTACAGAGTGTGTGCCAGC
Pvf1 N2 LF	TAGCGGCCGCGAATTTAAAAATGCGATTCGCTTCCTGGAA
Pvf1 N2 LR	CACCAAGGGCGAATTGATTACGGACGGTTGCTGGAGATTGG
Pvf1 N2 RF	TTCCAAGGGCGAATTAGCAACGCCGGCGAGCTG
Pvf1 N2 RR	AGGTTTAAACGAATTCAGAGTGTGTGCCAGCAGTTG
Pvf1 C1 LF	TAGCGGCCGCGAATTCACTTCCTCTGCGATCGTTTGC
Pvf1 C1 LR	CACCAAGGGCGAATTGGCAGCGGCACTGCGTATGC
Pvf1 C1 RF	TTCCAAGGGCGAATTAGATTGTAGGACCAAGGCGGAGGACTGCA
Pvf1 C1 RR	AGGTTTAAACGAATTTCCCATTTTTGCCTCAACTCAGC

Table S8. List of CRISPR knockin of HA tag in mature chemoattractant ligand peptide

	pU6-BbsI-chiRNA vector	pHD-2xHA-ScarlessDsRed vector	signal in live staining	signal in fixed staining	homozygous viable
Keren N1	pU6 KerenN	pHD KerenN1	yes	no	yes
Keren C1	pU6 KerenC	pHD KerenC1	no	no	no
Spitz N1	pU6 SpitzN	pHD SpitzN1	no	no	no
Spitz C1	pU6 SpitzC	pHD SpitzC1	no	no	no
PVF1 N1	pU6 PVF1N	pHD PVF1N1	no	N.A.	N.A.
PVF1 N2	pU6 PVF1N	pHD PVF1N2	no	yes	yes
PVF1 C1	pU6 PVF1C	pHD PVF1C1	no	no	no

Table S9. Adhesion energy cost for N-cell junctures (in unit of the adhesion strength A)

	$W_{adh,2}$	$W_{adh,3}$	$W_{adh,4}$	$W_{adh,5}$	$W_{adh,6}$	$W_{adh,7}$	$W_{adh,8}$
value	$6.3\,A$	$4.9\,A$	$3.8\,A$	$2.8\,A$	$1.9\,A$	$1.1\,A$	$0.3\,A$

Table S10. Model parameters.

	c_m	L	ξ	r_0	c_2	α	β_1	β_2
value	10	140 µm	42 µm	10 µm	1	80	0.4	0.2

Table S11. Parameter scanning of α and β_1. Values in the table correspond to posterior and medial migration index and are color coded with red/green corresponding to low/high values. The parameter values used in wild-type simulations are underlined.

% posterior		β_1										
		0	0.1	0.2	0.3	0.4	0.5	0.6	0.7	0.8	0.9	1
α	0	35	57	72	87	91	92	92	91	92	92	92
	10	37	57	76	87	91	92	92	92	92	92	92
	20	41	57	82	89	91	92	92	92	92	92	92
	30	42	59	78	91	92	92	92	93	92	92	92
	40	43	57	78	91	91	92	92	92	93	93	92
	50	46	61	76	89	91	92	92	92	92	92	92
	60	45	61	72	87	91	92	92	92	92	93	93
	70	46	58	74	84	90	92	92	92	93	92	93
	80	48	60	67	81	91	92	92	92	92	92	93
	90	49	59	70	79	86	92	92	92	93	93	92
	100	50	59	67	74	86	90	92	92	92	93	93

% medial		β_1										
		0	0.1	0.2	0.3	0.4	0.5	0.6	0.7	0.8	0.9	1
α	0	40	53	59	61	58	59	61	65	70	71	71
	10	58	60	63	66	67	74	73	73	74	72	76
	20	64	69	74	70	73	79	76	76	80	78	78
	30	71	74	78	77	77	81	78	81	82	84	79
	40	69	78	80	83	83	82	82	85	82	87	82
	50	83	82	82	83	84	84	87	84	87	87	85
	60	85	87	86	86	86	86	87	85	86	86	88
	70	88	87	88	86	87	88	88	88	88	88	89
	80	89	89	89	87	87	87	87	89	88	88	89
	90	88	88	89	88	87	89	89	89	90	89	89
	100	90	90	90	88	89	88	89	88	90	89	90

Multimedia Files

Movie S1. Confocal time-lapse imaging of normal border cell migration. SlboGal4 drives UAS-mCD8-EGFP (green) and UAS-RFPnls (magenta).

Movie S2. “Fly-through” from the anterior tip of the egg chamber where the border cells are located to the oocyte border, using near isotropic light sheet imaging showing the nurse cell membranes encountered by the border cells as they migrate. Multiple nurse cells meet in the center of the egg chamber where there is high membrane curvature. Border cells encounter ~40 side paths along the way. Green, E-cadherin. Magenta, F-actin. Scale bar, 20 μm.

Movie S3. Confocal time-lapse imaging of border cell migration with germline knockdown of E-cadherin. Matalpha4-Gal4;UAS-EcadRNAi. Green, Slbo-PHEGFP; magenta, UMAT-Lyn-tdTomato.

Movie S4. (Fig. 2E and F) (A) Confocal time-lapse imaging of a nurse cell juncture pulled by an incoming border cell cluster in a control egg chamber. Green, Slbo-PHEGFP; magenta, UMAT-Lyn-tdTomato, Ubi-HisRFP. Note that the juncture shown by the yellow filament is just an example. Other junctures that the border cells contact are also deflected. In the first and last time points, tracking is removed to show the original membrane signal. (B) Confocal time-lapse imaging of an egg chamber with germline knockdown of E-cadherin (Matalpha4-Gal4;UAS-EcadRNAi) showing absence of nurse cell membrane deflection when border cell protrusions touch nurse cell membranes. Despite touching the nurse cell juncture multiple times, the border cell protrusion did not deflect it (one juncture is highlighted by the yellow filament). In the first and last time points, tracking is removed to show the original membrane signal.

Movie S5. (fig. S11B, fig. S19A) Animation of 3-dimensional reconstruction of nurse cells and ring canals in a stage 9 egg chamber. White, F-actin; green, Slbo-LifeactGFP; blue, Hoechst. Nurse cell color indicates connection distance to the oocyte (red). White, border cells at the anterior tip. Yellow circles, ring canals. The egg chamber was stained to show F-actin (white), border cells (green), and nuclei (blue). First the reconstructed nurse cells rotate 360 degrees to show that nurse cells that connect closer to the oocyte (red) are located more posteriorly. Then the ring canals (yellow) are shown to display their location in between connected nurse cells.

Movie S6. (Fig. 3A and C) Animation of 3-dimensional reconstruction of different types of nurse cell contacts in a stage 9 egg chamber. Green, Slbo-LifeactGFP; white, F-actin or F-actin with outer follicle cell signal masked. Two-cell-contacts are shown as surfaces and color represents position along the z axis. Three-nurse cell junctures are represented as lines and color provides position in z. Magenta dots represent junctures of >3 nurse cells. First F-actin (white) and border cells (green) are shown. Then outer-follicle cell F-actin signals are masked to show nurse cell contacts. Then 2-cell surfaces are shown in 360 degree rotation, followed by >=3 cell juncture views in another 360 degree rotation.

Movie S7. (Fig. 4A) Simulation of border cell migration with nurse cell geometry and anterior-posterior chemoattractant gradient.

Movie S8. (fig. S17B and C). A confocal time-lapse movie of border cell migration in germline knockdown of E-cadherin. Border cells migrate along nurse-cell/nurse-cell/follicle-cell paths instead of nurse-cell/follicle-cell. Green, Slbo-PHEGFP; magenta, dextran.

Movie S9. (fig.S22A) A confocal time-lapse movie of wild-type border cell migration. Note the dorsal migration prior to reaching the oocyte boundary. Green, Slbo-PHEGFP; white, UMAT-Lyn-tdTomato.

Movie S10. (fig.S22C) Simulation of border cell migration with nurse cell geometry and anterior-posterior chemoattractant gradient and dorsal Grk gradient.

References

22. W. Dai, D. J. Montell, *Methods Mol. Biol.* **1407**, 153–168 (2016).

23. S. Preibisch *et al.*, *Nat. Methods*. **11**, 645–648 (2014).

24. I. Heemskerk, S. J. Streichan, *Nat. Methods*. **12**, 1139–1142 (2015).

25. D. Cai *et al.*, *Proc Natl Acad Sci USA*. **113**, E2134-41 (2016).

26. D. J. Montell, P. Rorth, A. C. Spradling, *Cell*. **71**, 51–62 (1992).

27. A. Cliffe *et al.*, *Nat. Commun.* **8**, 14905 (2017).

28. M. A. Lilly, A. C. Spradling, *Genes Dev.* **10**, 2514–2526 (1996).